

# Interrogating theoretical models of neural computation with deep inference

Sean R. Bittner<sup>1</sup>, Agostina Palmigiano<sup>1</sup>, Alex T. Piet<sup>2</sup>, Chunyu A. Duan<sup>3</sup>, Carlos D. Brody<sup>2</sup>, Kenneth D. Miller<sup>1</sup>, and John P. Cunningham<sup>4</sup>.

<sup>1</sup>Department of Neuroscience, Columbia University,

<sup>2</sup>Princeton Neuroscience Institute,

<sup>3</sup>Institute of Neuroscience, Chinese Academy of Sciences,

<sup>4</sup>Department of Statistics, Columbia University

## <sup>1</sup> 1 Abstract

<sup>2</sup> A cornerstone of theoretical neuroscience is the circuit model: a system of equations that captures  
<sup>3</sup> a hypothesized neural mechanism. Such models are valuable when they give rise to an experimen-  
<sup>4</sup> tally observed phenomenon – whether behavioral or in terms of neural activity – and thus can  
<sup>5</sup> offer insights into neural computation. The operation of these circuits, like all models, critically  
<sup>6</sup> depends on the choices of model parameters. Historically, the gold standard has been to analyt-  
<sup>7</sup> ically derive the relationship between model parameters and computational properties. However,  
<sup>8</sup> this enterprise quickly becomes infeasible as biologically realistic constraints are included into the  
<sup>9</sup> model increasing its complexity, often resulting in *ad hoc* approaches to understanding the relation-  
<sup>10</sup> ship between model and computation. We bring recent machine learning techniques – the use of  
<sup>11</sup> deep generative models for probabilistic inference – to bear on this problem, learning distributions  
<sup>12</sup> of parameters that produce the specified properties of computation. Importantly, the techniques  
<sup>13</sup> we introduce offer a principled means to understand the implications of model parameter choices  
<sup>14</sup> on computational properties of interest. We motivate this methodology with a worked example  
<sup>15</sup> analyzing sensitivity in the stomatogastric ganglion. We then use it to go beyond linear theory  
<sup>16</sup> of neuron-type input-responsivity in a model of primary visual cortex, gain a mechanistic under-  
<sup>17</sup> standing of rapid task switching in superior colliculus models, and attribute error to connectivity  
<sup>18</sup> properties in recurrent neural networks solving a simple mathematical task. More generally, this  
<sup>19</sup> work suggests a departure from realism vs tractability considerations, towards the use of modern  
<sup>20</sup> machine learning for sophisticated interrogation of biologically relevant models.

## 21 2 Introduction

22 The fundamental practice of theoretical neuroscience is to use a mathematical model to understand  
23 neural computation, whether that computation enables perception, action, or some intermediate  
24 processing [1]. A neural computation is systematized with a set of equations – the model – and  
25 these equations are motivated by biophysics, neurophysiology, and other conceptual considerations.  
26 The function of this system is governed by the choice of model parameters, which when configured  
27 in a particular way, give rise to a measurable signature of a computation. The work of analyzing a  
28 model then requires solving the inverse problem: given a computation of interest, how can we reason  
29 about these particular parameter configurations? The inverse problem is crucial for reasoning about  
30 likely parameter values, uniquenesses and degeneracies, attractor states and phase transitions, and  
31 predictions made by the model.

32 Consider the idealized practice: one carefully designs a model and analytically derives how model  
33 parameters govern the computation. Seminal examples of this gold standard (which often adopt  
34 approaches from statistical physics) include our field’s understanding of memory capacity in asso-  
35 ciative neural networks [2], chaos and autocorrelation timescales in random neural networks [3],  
36 the paradoxical effect [4], and decision making [5]. Unfortunately, as circuit models include more  
37 biological realism, theory via analytical derivation becomes intractable. This creates an unfavor-  
38 able tradeoff. On the one hand, one may tractably analyze systems of equations with unrealistic  
39 assumptions (for example symmetry or gaussianity), mathematically formalizing how parameters  
40 affect computation in a too-simple model. On the other hand, one may choose a more biologically  
41 accurate, scientifically relevant model at the cost of *ad hoc* approaches to analysis (such as sim-  
42 ply examining simulated activity), potentially resulting in bad inference of parameters and thus  
43 erroneous scientific predictions or conclusions.

44 Of course, this same tradeoff has been confronted in many scientific fields characterized by the  
45 need to do inference in complex models. In response, the machine learning community has made  
46 remarkable progress in recent years, via the use of deep neural networks as a powerful inference  
47 engine: a flexible function family that can map observed phenomena (in this case the measurable  
48 signal of some computation) back to probability distributions quantifying the likely parameter  
49 configurations. One celebrated example of this approach from machine learning, of which we  
50 draw key inspiration for this work, is the variational autoencoder [6, 7], which uses a deep neural  
51 network to induce an (approximate) posterior distribution on hidden variables in a latent variable

model, given data. Indeed, these tools have been used to great success in neuroscience as well, in particular for interrogating parameters (sometimes treated as hidden states) in models of both cortical population activity [8, 9, 10, 11] and animal behavior [12, 13, 14]. These works have used deep neural networks to expand the expressivity and accuracy of statistical models of neural data [15].

However, these inference tools have not significantly influenced the study of theoretical neuroscience models, for at least three reasons. First, at a practical level, the nonlinearities and dynamics of many theoretical models are such that conventional inference tools typically produce a narrow set of insights into these models. Indeed, only in the last few years has deep learning research advanced to a point of relevance to this class of problem. Second, the object of interest from a theoretical model is not typically data itself, but rather a qualitative phenomenon – inspection of model behavior, or better, a measurable signature of some computation – an *emergent property* of the model. Third, because theoreticians work carefully to construct a model that has biological relevance, such a model as a result often does not fit cleanly into the framing of a statistical model. Technically, because many such models stipulate a noisy system of differential equations that can only be sampled or realized through forward simulation, they lack the explicit likelihood and priors central to the probabilistic modeling toolkit.

To address these three challenges, we developed an inference methodology – ‘emergent property inference’ – which learns a distribution over parameter configurations in a theoretical model. This distribution has two critical properties: (*i*) it is chosen such that draws from the distribution (parameter configurations) correspond to systems of equations that give rise to a specified emergent property (a set of constraints); and (*ii*) it is chosen to have maximum entropy given those constraints, such that we identify all likely parameters and can use the distribution to reason about parametric sensitivity and degeneracies [16]. First, we stipulate a bijective deep neural network that induces a flexible family of probability distributions over model parameterizations with a probability density we can calculate [17, 18, 19]. Second, we quantify the notion of emergent properties as a set of moment constraints on datasets generated by the model. Thus, an emergent property is not a single data realization, but a phenomenon or a feature of the model, which is ultimately the object of interest in theoretical neuroscience. Conditioning on an emergent property requires a variant of deep probabilistic inference methods, which we have previously introduced [20]. Third, because we can not assume the theoretical model has explicit likelihood on data or the emergent property of interest, we use stochastic gradient techniques in the spirit of likelihood free variational inference

[21]. Taken together, emergent property inference (EPI) provides a methodology for inferring parameter configurations consistent with a particular emergent phenomena in theoretical models. We use a classic example of parametric degeneracy in a biological system, the stomatogastric ganglion [22], to motivate and clarify the technical details of EPI.

Equipped with this methodology, we then investigated three models of current importance in theoretical neuroscience. These models were chosen to demonstrate generality through ranges of biological realism (from conductance-based biophysics to recurrent neural networks), neural system function (from pattern generation to abstract cognitive function), and network scale (from four to infinite neurons). First, we use EPI to produce a set of verifiable hypotheses of input-responsivity in a four neuron-type dynamical model of primary visual cortex; we then validate these hypotheses in the model. Second, we demonstrated how the systematic application of EPI to levels of task performance can generate experimentally testable hypotheses regarding connectivity in superior colliculus. Third, we use EPI to uncover the sources of error in a low-rank recurrent neural network executing a simple mathematical task. The novel scientific insights offered by EPI contextualize and clarify the previous studies exploring these models [23, 24, 25, 26], and more generally, these results point to the value of deep inference for the interrogation of biologically relevant models.

We note that, during our preparation and early presentation of this work [27, 28], another work has arisen with broadly similar goals: bringing statistical inference to mechanistic models of neural circuits [29, 30]. We are encouraged by this general problem being recognized by others in the community, and we emphasize that these works offer complementary neuroscientific contributions (different theoretical models of focus) and use different technical methodologies (ours is built on our prior work [20], theirs similarly [31]). These distinct methodologies and scientific investigations emphasize the increased importance and timeliness of both works.

## 3 Results

### 3.1 Motivating emergent property inference of theoretical models

Consideration of the typical workflow of theoretical modeling clarifies the need for emergent property inference. First, one designs or chooses an existing model that, it is hypothesized, captures the computation of interest. To ground this process in a well-known example, consider the stomatogastric ganglion (STG) of crustaceans, a small neural circuit which generates multiple rhythmic muscle activation patterns for digestion [32]. Despite full knowledge of STG connectivity and a

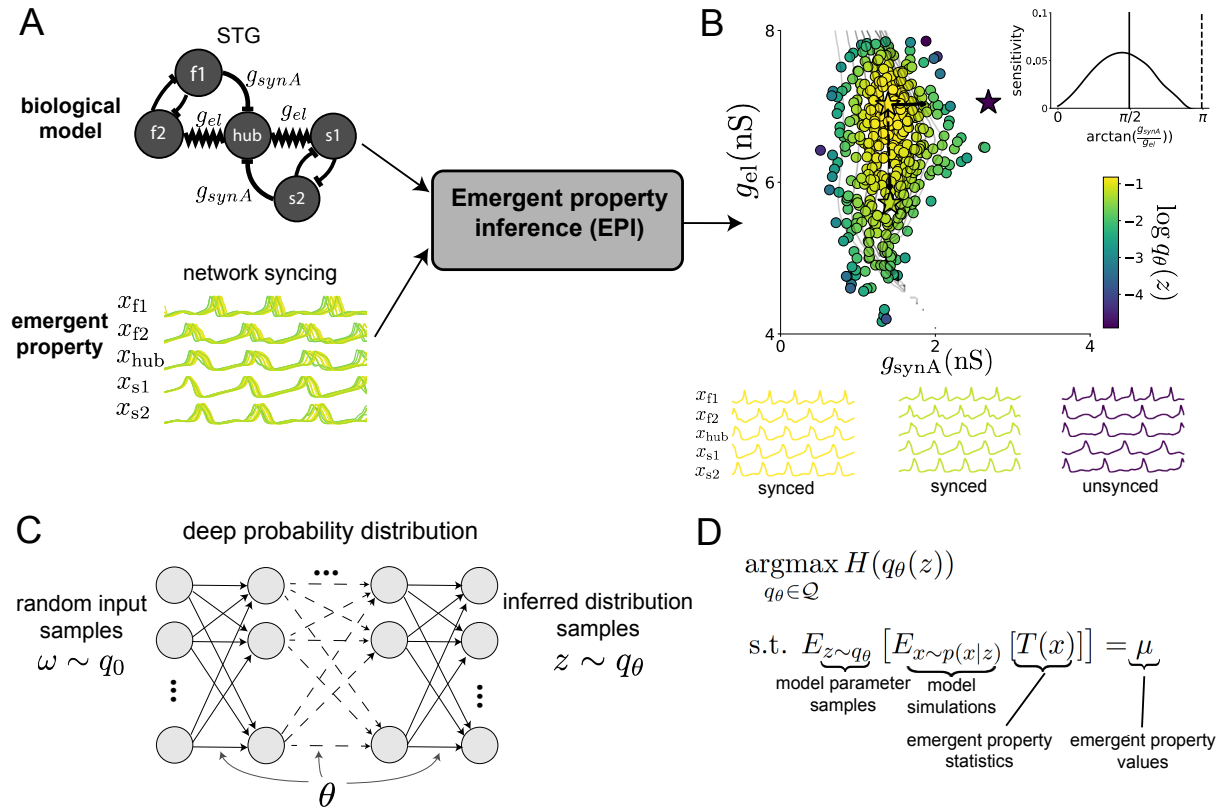


Figure 1: Emergent property inference (EPI) in the stomatogastric ganglion. A. For a choice of model (STG) and emergent property (network syncing), emergent property inference (EPI, gray box) learns a distribution of the model parameters  $z = [g_{el}, g_{synA}]$  producing network syncing. In the STG model, jagged connections indicate electrical coupling having electrical conductance  $g_{el}$ . Other connections in the diagram are inhibitory synaptic projections having strength  $g_{synA}$  onto the hub neuron, and  $g_{synB} = 5\text{nS}$  for mutual inhibitory connections. Network syncing traces are colored by log probability density of their generating parameters (stars) in the EPI-inferred distribution. B. The EPI distribution of STG model parameters producing network syncing. Samples are colored by log probability density. Distribution contours of emergent property value error are shown at levels of  $5 \times 10^{-7}$  and  $1 \times 10^{-6}$  (dark and light gray). Eigenvectors of the Hessian at the mode of the inferred distribution are indicated as  $v_1$  (solid) and  $v_2$  (dashed) with lengths scaled by the square root of the absolute value of their eigenvalues. Simulated activity is shown for three samples (stars). (Inset) Sensitivity of the system with respect to network syncing along all dimensions of parameter space away from the mode. (see Section B.2.1). C. Deep probability distributions map a latent random variable  $w$  through a deep neural network with weights and biases  $\theta$  to parameters  $z = f_\theta(w)$  distributed as  $q_\theta(z)$ . D. EPI optimization: To learn the EPI distribution  $q_\theta(z)$  of model parameters that produce an emergent property, the emergent property statistics  $T(x)$  are set in expectation over model parameter samples  $z \sim q_\theta(z)$  and model simulations  $x \sim p(x | z)$  to emergent property values  $\mu$ .

114 precise characterization of its rhythmic pattern generation, biophysical models of the STG have  
 115 complicated relationships between circuit parameters and neural activity [22, 33]. A model of the  
 116 STG [23] is shown schematically in Figure 1A, and note that the behavior of this model will be crit-  
 117 ically dependent on its parameterization – the choices of conductance parameters  $z = [g_{el}, g_{synA}]$ .  
 118 Specifically, the two fast neurons ( $f_1$  and  $f_2$ ) mutually inhibit one another, and oscillate at a faster  
 119 frequency than the mutually inhibiting slow neurons ( $s_1$  and  $s_2$ ). The hub neuron (hub) couples  
 120 with either the fast or slow population or both.  
 121 Second, once the model is selected, one defines the emergent property, the measurable signal of  
 122 scientific interest. To continue our running STG example, one such emergent property is the  
 123 phenomenon of *network syncing* – in certain parameter regimes, the frequency of the hub neuron  
 124 matches that of the fast and slow populations at an intermediate frequency. This emergent property  
 125 is shown in Figure 1A at a frequency of 0.53Hz.  
 126 Third, qualitative parameter analysis ensues: since precise mathematical analysis is intractable in  
 127 this model, a brute force sweep of parameters is done [23]. Subsequently, a qualitative description  
 128 is formulated to describe the different parameter configurations that lead to the emergent property.  
 129 In this last step lies the opportunity for a precise quantification of the emergent property as a  
 130 statistical feature of the model. Once we have such a methodology, we can infer a probability  
 131 distribution over parameter configurations that produce this emergent property.  
 132 Before presenting technical details (in the following section), let us understand emergent property  
 133 inference schematically: EPI (Fig. 1A gray box) takes, as input, the model and the specified  
 134 emergent property, and as its output, produces the parameter distribution shown in Figure 1B.  
 135 This distribution – represented for clarity as samples from the distribution – is then a scientifically  
 136 meaningful and mathematically tractable object. In the STG model, this distribution can be  
 137 specifically queried to reveal the prototypical parameter configuration for network syncing (the  
 138 mode; Figure 1B yellow star), and how network syncing decays based on changes away from the  
 139 mode. The eigenvectors (of the Hessian of the distribution at the mode) quantitatively formalize  
 140 the robustness of network syncing (Fig. 1B  $v_1$  and  $v_2$ ). Indeed, samples equidistant from the  
 141 mode along these EPI-identified dimensions of sensitivity ( $v_1$ ) and degeneracy ( $v_2$ ) agree with  
 142 error contours (Fig. 1B, contours) and have diminished or preserved network syncing, respectively  
 143 (Figure 1B inset and activity traces).

---

### 144 3.2 A deep generative modeling approach to emergent property inference

145 Emergent property inference (EPI) systematizes the three-step procedure of the previous section.  
 146 First, we consider the model as a coupled set of differential (and potentially stochastic) equations  
 147 [23]. In the running STG example, the model activity  $x = [x_{f1}, x_{f2}, x_{hub}, x_{s1}, x_{s2}]$  is the membrane  
 148 potential for each neuron, which evolves according to the biophysical conductance-based equation:

$$C_m \frac{dx}{dt} = -h(x; z) = -[h_{leak}(x; z) + h_{Ca}(x; z) + h_K(x; z) + h_{hyp}(x; z) + h_{elec}(x; z) + h_{syn}(x; z)] \quad (1)$$

149 where  $C_m = 1\text{nF}$ , and  $h_{leak}$ ,  $h_{Ca}$ ,  $h_K$ ,  $h_{hyp}$ ,  $h_{elec}$ , and  $h_{syn}$  are the leak, calcium, potassium, hyper-  
 150 polarization, electrical, and synaptic currents, all of which have their own complicated dependence  
 151 on  $x$  and  $z = [g_{el}, g_{synA}]$  (see Section B.2.1).

152 Second, we define the emergent property, which as above is network syncing: oscillation of the  
 153 entire population at an intermediate frequency of our choosing (Figure 1A bottom). Quantifying  
 154 this phenomenon is straightforward: we define network syncing to be that each neuron’s spiking  
 155 frequency – denoted  $\omega_{f1}(x)$ ,  $\omega_{f2}(x)$ , etc. – is close to an intermediate frequency of 0.53Hz. Math-  
 156 ematically, we achieve this via constraints on the mean and variance of  $\omega_\alpha(x)$  for each neuron  
 157  $\alpha \in \{f1, f2, hub, s1, s2\}$ :

$$\mathbb{E}[T(x)] \triangleq \mathbb{E} \begin{bmatrix} \omega_{f1}(x) \\ \vdots \\ (\omega_{f1}(x) - 0.53)^2 \\ \vdots \end{bmatrix} = \begin{bmatrix} 0.53 \\ \vdots \\ 0.025^2 \\ \vdots \end{bmatrix} \triangleq \mu, \quad (2)$$

158 which completes the quantification of the emergent property.

159 Third, we perform emergent property inference: we find a distribution over parameter configura-  
 160 tions  $z$ , and insist that samples from this distribution produce the emergent property; in other  
 161 words, they obey the constraints introduced in Equation 2. This distribution will be chosen from  
 162 a family of probability distributions  $\mathcal{Q} = \{q_\theta(z) : \theta \in \Theta\}$ , defined by a deep generative distribution  
 163 of the normalizing flow class [17, 18, 19] – neural networks which transform a simple distribution  
 164 into a suitably complicated distribution (as is needed here). This deep distribution is represented  
 165 in Figure 1C (see Section B.1). Then, mathematically, we must solve the following optimization  
 166 program:

$$\begin{aligned} & \underset{q_\theta \in \mathcal{Q}}{\operatorname{argmax}} H(q_\theta(z)) \\ & \text{s.t. } \mathbb{E}_{z \sim q_\theta} [\mathbb{E}_{x \sim p(x|z)} [T(x)]] = \mu, \end{aligned} \quad (3)$$

where  $T(x), \mu$  are defined as in Equation 2, and  $p(x|z)$  is the intractable distribution of data from the model,  $x$ , given that model's parameters  $z$  (we access samples from this distribution by running the model forward). The purpose of each element in this program is detailed in Figure 1D. Finally, we recognize that many distributions in  $\mathcal{Q}$  will respect the emergent property constraints, so we require a normative principle to select amongst them. This principle is captured in Equation 3 by the primal objective  $H$ . Here we chose Shannon entropy as a means to find parameter distributions with minimal assumptions beyond some chosen structure [34, 35, 20, 36], but we emphasize that the EPI method is unaffected by this choice (but the results of course will depend on the primal objective chosen).

EPI optimizes the weights and biases  $\theta$  of the deep neural network (which induces the probability distribution) by iteratively solving Equation 3. The optimization is complete when the sampled models with parameters  $z \sim q_\theta$  produce activity consistent with the specified emergent property (Fig. S4). Such convergence is evaluated with a hypothesis test that the mean of each emergent property statistic is not different than its emergent property value (see Section B.1.2). Further validation of EPI is available in the supplementary materials, where we analyze a simpler model for which ground-truth statements can be made (Section B.1.1). In relation to broader methodology, inspection of the EPI objective reveals a natural relationship to posterior inference. Specifically, EPI executes variational inference in an exponential family model, the sufficient statistics and mean parameter of which are defined by the emergent property statistics and values, respectively (see Section B.1.4). Equipped with this method, we now prove out the value of EPI by using it to investigate and produce novel insights about three prominent models in neuroscience.

### 3.3 Comprehensive input-responsivity in a nonlinear sensory system

Dynamical models of excitatory (E) and inhibitory (I) populations with supralinear input-output function have succeeded in explaining a host of experimentally documented phenomena. In a regime characterized by inhibitory stabilization of strong recurrent excitation, these models give rise to paradoxical responses [4], selective amplification [37], surround suppression [38] and normalization [39]. Despite their strong predictive power, E-I circuit models rely on the assumption that inhibition can be studied as an indivisible unit. However, experimental evidence shows that inhibition is composed of distinct elements – parvalbumin (P), somatostatin (S), VIP (V) – composing 80% of GABAergic interneurons in V1 [40, 41, 42], and that these inhibitory cell types follow specific connectivity patterns (Fig. 2A) [43]. Recent theoretical advances [24, 44, 45], have only started

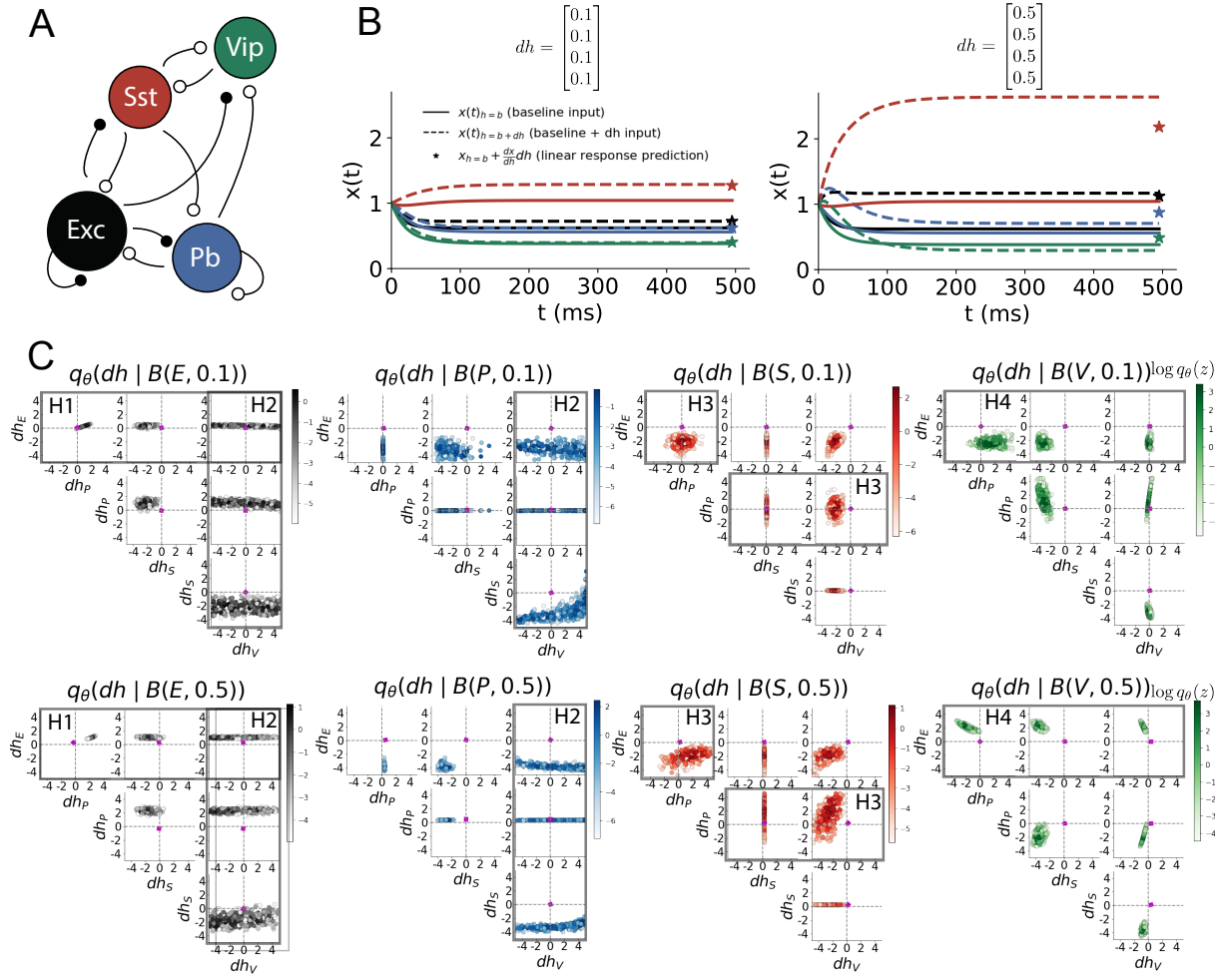


Figure 2: Hypothesis generation through EPI in a V1 model. A. Four-population model of primary visual cortex with excitatory (black), parvalbumin (blue), somatostatin (red), and VIP (green) neurons. Some neuron-types largely do not form synaptic projections to others (excitatory and inhibitory projections filled and unfilled, respectively). B. V1 model simulations for input (solid)  $h = b$  and (dashed)  $h = b + dh$ . Stars indicate the linear response prediction. C. EPI distributions on differential input  $dh$  conditioned on differential response  $\mathcal{B}(\alpha, y)$ . Supporting evidence for the four generated hypotheses are indicated by gray boxes with labels H1, H2, H3, and H4. The linear prediction from two standard deviations away from  $y$  (from negative to positive) is overlaid in magenta (very small, near origin).

198 to address the consequences of this multiplicity in the dynamics of V1, strongly relying on linear  
 199 theoretical tools. Here, we go beyond linear theory by systematically generating and evaluating hy-  
 200 potheses of circuit model function using EPI distributions of neuron-type inputs producing various  
 201 neuron-type population responses.

202 Specifically, we consider a four-dimensional circuit model with dynamical state given by the firing  
 203 rate  $x$  of each neuron-type population  $x = [x_E, x_P, x_S, x_V]^\top$ . Given a time constant of  $\tau = 20$  ms  
 204 and a power  $n = 2$ , the dynamics are driven by the rectified and exponentiated sum of recurrent  
 205 ( $Wx$ ) and external  $h$  inputs:

$$\tau \frac{dx}{dt} = -x + [Wx + h]_+^n. \quad (4)$$

206 The effective connectivity weights  $W$  were obtained from experimental recordings of publicly avail-  
 207 able datasets of mouse V1 [46, 47] (see Section B.2.2). The input  $h = b + dh$  is comprised of a  
 208 baseline input  $b = [b_E, b_P, b_S, b_V]^\top$  and a differential input  $dh = [dh_E, dh_P, dh_S, dh_V]^\top$  to each  
 209 neuron-type population. Throughout subsequent analyses, the baseline input is  $b = [1, 1, 1, 1]^\top$ .

210 With this model, we are interested in the differential responses of each neuron-type population to  
 211 changes in input  $dh$ . Initially, we studied the linearized response of the system to input  $\frac{dx_{ss}}{dh}$  at the  
 212 steady state response  $x_{ss}$ , i.e. a fixed point. All analyses of this model consider the steady state  
 213 response, so we drop the notation  $ss$  from here on. While this linearization accurately predicts  
 214 differential responses  $dx = [dx_E, dx_P, dx_S, dx_V]$  for small differential inputs to each population  
 215  $dh = [0.1, 0.1, 0.1, 0.1]$  (Fig 2B left), the linearization is a poor predictor in this nonlinear model  
 216 more generally (Fig. 2B right). Currently available approaches to deriving the steady state response  
 217 of the system are limited.

218 To get a more comprehensive picture of the input-responsivity of each neuron-type beyond linear  
 219 theory, we used EPI to learn a distribution of the differential inputs to each population  $dh$  that  
 220 produce an increase of  $y$  in the rate of each neuron-type population  $\alpha \in \{E, P, S, V\}$ . We want  
 221 to know the differential inputs  $dh$  that result in a differential steady state  $dx_\alpha$  (the change in  $x_\alpha$   
 222 when receiving input  $h = b + dh$  with respect to the baseline  $h = b$ ) of value  $y$  with some small,  
 223 arbitrarily chosen amount of variance  $0.01^2$ . These statements amount to the emergent property

$$\mathcal{B}(\alpha, y) \triangleq \mathbb{E} \begin{bmatrix} dx_\alpha \\ (dx_\alpha - y)^2 \end{bmatrix} = \begin{bmatrix} y \\ 0.01^2 \end{bmatrix} \quad (5)$$

224 We maintain the notation  $\mathcal{B}(\cdot)$  throughout the rest of the study as short hand for emergent property,

which represents a different signature of computation in each application.

Using EPI, we inferred the distribution of  $dh$  shown in Figure 2C producing  $\mathcal{B}(\alpha, y)$ . Columns correspond to inferred distributions of excitatory ( $\alpha = E$ , red), parvalbumin ( $\alpha = P$ , blue), somatostatin ( $\alpha = S$ , red) and VIP ( $\alpha = V$ , green) neuron-type response increases, while each row corresponds to increase amounts of  $y \in \{0.1, 0.5\}$ . For each pair of parameters, we show the two-dimensional marginal distribution of samples colored by  $\log q_\theta(dh | \mathcal{B}(\alpha, y))$ . The inferred distributions immediately suggest four hypotheses:

232

- 233 H1: as is intuitive, each neuron-type's firing rate should be sensitive to that neuron-type's  
234 direct input (e.g. Fig. 2C H1 gray boxes indicate low variance in  $dh_E$  when  $\alpha = E$ . Same  
235 observation in all inferred distributions);
- 236 H2: the E- and P-populations should be largely unaffected by input to the V-population (Fig.  
237 2C H2 gray boxes indicate high variance in  $dh_V$  when  $\alpha \in \{E, P\}$ );
- 238 H3: the S-population should be largely unaffected by input to the P-population (Fig. 2C H3  
239 gray boxes indicate high variance in  $dh_P$  when  $\alpha = S$ );
- 240 H4: there should be a nonmonotonic response of the V-population with input to the E-  
241 population (Fig. 2C H4 gray boxes indicate that negative  $dh_E$  should result in small  $dx_V$ ,  
242 but positive  $dh_E$  should elicit a larger  $dx_V$ );

243 We evaluate these hypotheses by taking steps in individual neuron-type input  $\delta h_\alpha$  away from the  
244 modes of the inferred distributions at  $y = 0.1$

$$dh^* = z^* = \underset{z}{\operatorname{argmax}} \log q_\theta(z | \mathcal{B}(\alpha, 0.1)). \quad (6)$$

245 Here  $\delta x_\alpha$  is the change in steady state response to the system with input  $h = b + dh^* + \delta h_\alpha \hat{u}_\alpha$   
246 compared to  $h = b + dh^*$ , where  $\hat{u}_\alpha$  is a unit vector in the dimension of  $\alpha$ . The EPI-generated  
247 hypotheses are confirmed:

- 248 H1: the neuron-type responses are sensitive to their direct inputs (Fig. 3A black, 3B blue,  
249 3C red, 3D green);
- 250 H2: the E- and P-populations are not affected by  $\delta h_V$  (Fig. 3A green, 3B green);
- 251 H3: the S-population is not affected by  $\delta h_P$  (Fig. 3C blue);
- 252 H4: the V-population exhibits a nonmonotonic response to  $\delta h_E$  (Fig. 3D black), and is in  
253 fact the only population to do so (Fig. 3A-C black).

254 These hypotheses were in stark contrast to what was available to us via traditional analytical

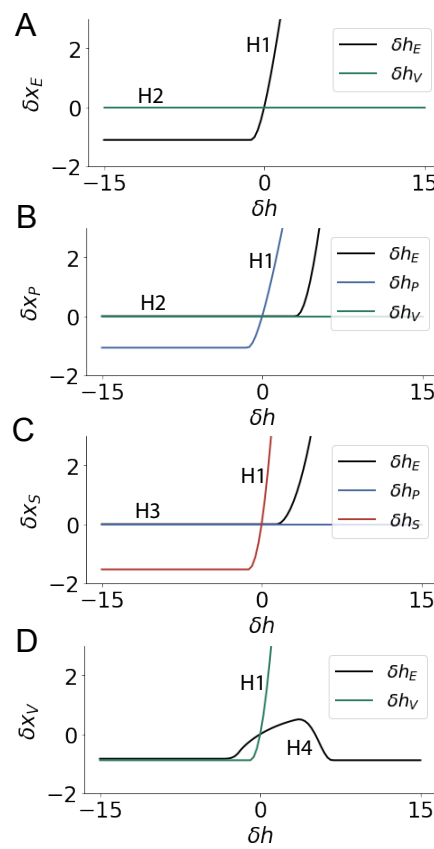


Figure 3: Confirming EPI generated hypotheses in V1. A. Differential responses  $\delta x_E$  by the E-population to changes in individual input  $\delta h_\alpha \hat{u}_\alpha$  away from the mode of the EPI distribution  $dh^*$ . B-D Same plots for the P-, S-, and V-populations. Labels H1, H2, H3, and H4 indicate which curves confirm which hypotheses.

255 linear prediction (Fig. 2C, magenta, see Section B.2.2). To this point, we have shown the utility of  
 256 EPI on relatively low-level emergent properties like network syncing and differential neuron-type  
 257 population responses. In the remainder of the study, we focus on using EPI to understand models  
 258 of more abstract cognitive function.

### 259 3.4 Identifying neural mechanisms of flexible task switching

260 In a rapid task switching experiment [48], rats were explicitly cued on each trial to either orient  
 261 towards a visual stimulus in the Pro (P) task or orient away from a visual stimulus in the Anti  
 262 (A) task (Fig. 4a). Neural recordings in the midbrain superior colliculus (SC) exhibited two  
 263 populations of neurons that simultaneously represented both task context (Pro or Anti) and motor  
 264 response (contralateral or ipsilateral to the recorded side): the Pro/Contra and Anti/Ipsi neurons  
 265 [25]. Duan et al. proposed a model of SC that, like the V1 model analyzed in the previous section, is  
 266 a four-population dynamical system. We analyzed this model, where the neuron-type populations  
 267 are functionally-defined as the Pro- and Anti-populations in each hemisphere (left (L) and right  
 268 (R)), their connectivity is parameterized geometrically (Fig. 4B). The input-output function of this

269 model is chosen such that the population responses  $x = [x_{LP} \ x_{LA} \ x_{RP} \ x_{RA}]^\top$  are bounded  
 270 from 0 to 1 giving rise to high (1) or low (0) responses at the end of the trial:

$$x_\alpha = \left( \frac{1}{2} \tanh \left( \frac{u_\alpha - \epsilon}{\zeta} \right) + \frac{1}{2} \right) \quad (7)$$

271 where  $\epsilon = 0.05$  and  $\zeta = 0.5$ . The dynamics evolve with timescale  $\tau = 0.09$  via an internal variable  
 272  $u$  governed by connectivity weights  $W$

$$\tau \frac{du}{dt} = -u + Wx + h + \sigma dB \quad (8)$$

273 with gaussian noise of variance  $\sigma^2 = 1$ . The input  $h$  is comprised of a cue-dependent input to the  
 274 Pro or Anti populations, a stimulus orientation input to either the Left or Right populations, and  
 275 a choice-period input to the entire network (see Section B.2.3). Here, we use EPI to determine the  
 276 changes in network connectivity  $z = [sW_P \ sW_A \ vW_{PA} \ vW_{AP} \ dW_{PA} \ dW_{AP} \ hW_P \ hW_A]$   
 277 resulting in greater levels of rapid task switching accuracy.

278 To quantify the emergent property of rapid task switching at various levels of accuracy, we consid-  
 279 ered the requirements of this model in this behavioral paradigm. At the end of successful trials,  
 280 the response of the Pro population in the hemisphere of the correct choice must have a value near  
 281 1, while the Pro population in the opposite hemisphere must have a value near 0. Constraining a  
 282 population response  $x_\alpha \in [0, 1]$  to be either 0 or 1 can be achieved by requiring that it has Bernoulli  
 283 variance (see Section B.2.3). Thus, we can formulate rapid task switching at a level of accuracy  
 284  $p \in [0, 1]$  in both tasks in terms of the average steady response of the Pro population  $\hat{p}$  of the  
 285 correct choice, the error in Bernoulli variance of that Pro neuron  $\sigma_{err}^2$ , and the average difference  
 286 in Pro neuron responses  $d$  in both Pro and Anti trials:

$$\mathcal{B}(p) \triangleq \mathbb{E} \begin{bmatrix} \hat{p}_P \\ \hat{p}_A \\ (\hat{p}_P - p)^2 \\ (\hat{p}_A - p)^2 \\ \sigma_{P,err}^2 \\ \sigma_{A,err}^2 \\ d_P \\ d_A \end{bmatrix} = \begin{bmatrix} p \\ p \\ 0.15^2 \\ 0.15^2 \\ 0 \\ 0 \\ 1 \\ 1 \end{bmatrix} \quad (9)$$

287 Thus,  $\mathcal{B}(p)$  denotes Bernoulli, winner-take-all responses between Pro neurons in a model executing  
 288 rapid task switching near accuracy level  $p$ .

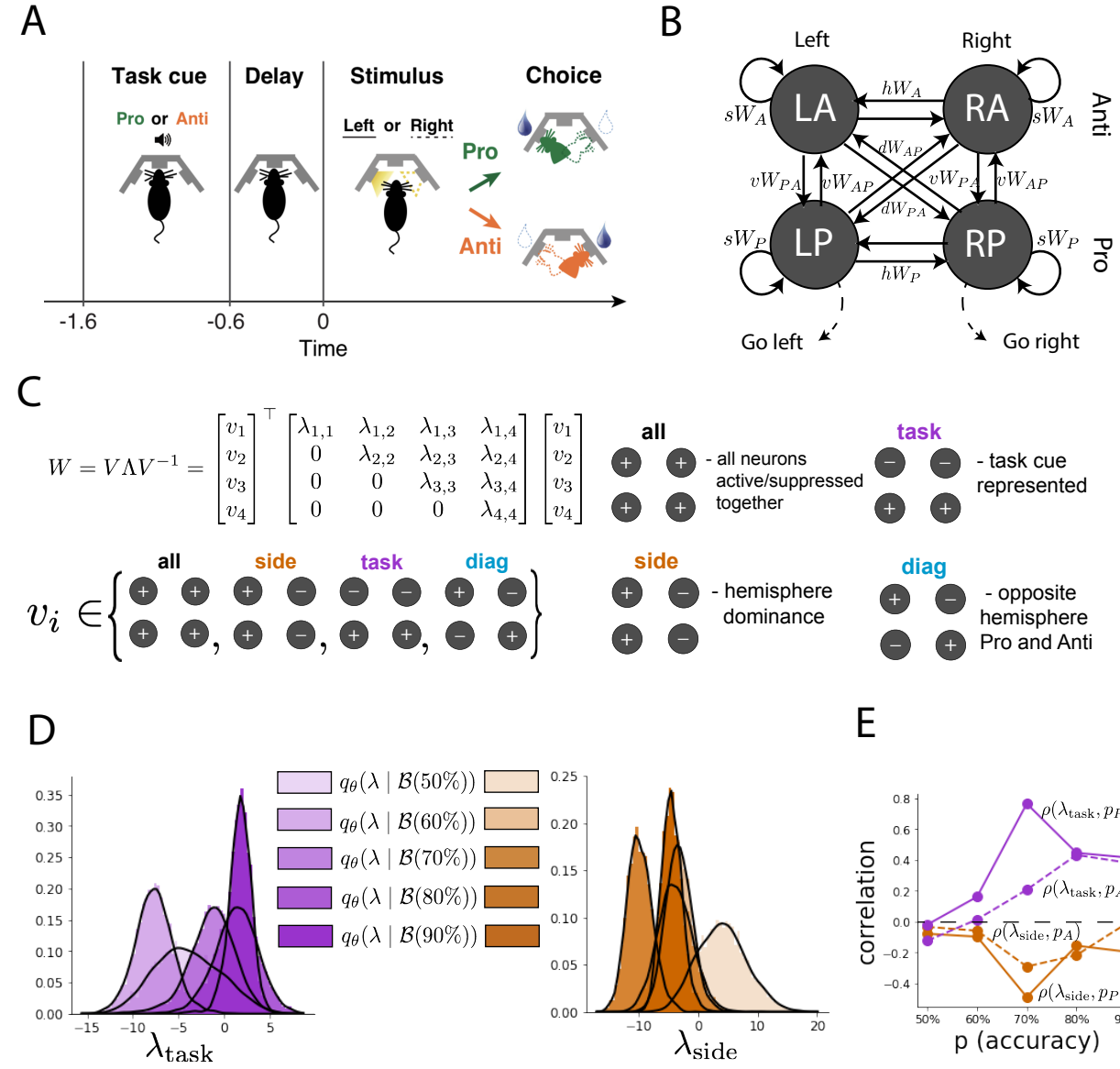


Figure 4: EPI reveals changes in SC [25] connectivity that control task accuracy. A. Rapid task switching behavioral paradigm (see text). B. Model of superior colliculus (SC). Neurons: LP - left pro, RP - right pro, LA - left anti, RA - right anti. Parameters:  $sW$  - self,  $hW$  - horizontal,  $vW$  - vertical,  $dW$  - diagonal weights. Subscripts  $P$  and  $A$  of connectivity weights indicate Pro or Anti populations, and e.g.  $vW_{PA}$  is a vertical weight from an Anti to a Pro population. C. The Schur decomposition of the weight matrix  $W = V \Lambda V^{-1}$  is a unique decomposition with orthogonal  $V$  and upper triangular  $\Lambda$ . Schur modes:  $v_{\text{all}}$ ,  $v_{\text{task}}$ ,  $v_{\text{side}}$ , and  $v_{\text{diag}}$ . D. The marginal EPI distributions of the Schur eigenvalues at each level of task accuracy. E. The correlation of Schur eigenvalue with task performance in each learned EPI distribution.

We used EPI to learn distributions of the SC weight matrix parameters  $z$  conditioned on various levels of rapid task switching accuracy  $\mathcal{B}(p)$  for  $p \in \{50\%, 60\%, 70\%, 80\%, 90\%\}$ . To make sense of these inferred distributions, we followed the approach of Duan et al. by decomposing the connectivity matrix  $W = V\Lambda V^{-1}$  in such a way (the Schur decomposition) that the basis vectors  $v_i$  are the same for all  $W$  (Fig. 4C). These basis vectors have intuitive roles in processing for this task, and are accordingly named the *all* mode - all neurons co-fluctuate, *side* mode - one side dominates the other, *task* mode - the Pro or Anti populations dominate the other, and *diag* mode - Pro- and Anti-populations of opposite hemispheres dominate the opposite pair. The corresponding eigenvalues (e.g.  $\lambda_{\text{task}}$ , which change according to  $W$ ) indicate the degree to which activity along that mode is increased or decreased by  $W$ .

We found that for greater task accuracies, the task mode eigenvalue increases, indicating the importance of  $W$  to the task representation (Fig. 4D, purple). Stepping from random chance (50%) networks to marginally task-performing (60%) networks, there is a marked decrease of the side mode eigenvalues (Fig. 4D, orange). Such side mode suppression remains in the models achieving greater accuracy, revealing its importance towards task performance. There were no interesting trends with task accuracy in the all or diag mode (hence not shown in Fig. 4). Importantly, we can conclude from our methodology that side mode suppression in  $W$  allows rapid task switching, and that greater task-mode representations in  $W$  increase accuracy. These hypotheses are confirmed by forward simulation of the SC model (Fig. 4E) suggesting experimentally testable predictions: increase in rapid task switching performance should be correlated with changes in effective connectivity resulting in an increase in task mode and decrease in side mode eigenvalues.

### 3.5 Linking RNN connectivity to error

So far, each model we have studied was designed from fundamental biophysical principles, genetically- or functionally-defined neuron types. At a more abstract level of modeling, recurrent neural networks (RNNs) are high-dimensional dynamical models of computation that are becoming increasingly popular in neuroscience research [49]. In theoretical neuroscience, RNN dynamics usually follow the equation

$$\frac{dx}{dt} = -x + W\phi(x) + h, \quad (10)$$

where  $x$  is the network activity,  $W$  is the network connectivity,  $\phi(\cdot) = \tanh(\cdot)$ , and  $h$  is the input to the system. Such RNNs are trained to do a task from a systems neuroscience experiment, and then the unit activations of the trained RNN are compared to recorded neural activity. Fully-connected

319 RNNs with tens of thousands of parameters are challenging to characterize [50], especially making  
 320 statistical inferences about their parameterization. Alternatively, we considered a rank-1,  $N$ -neuron  
 321 RNN with connectivity

$$W = g\chi + \frac{1}{N}mn^\top, \quad (11)$$

322 where  $\chi_{i,j} \sim \mathcal{N}(0, \frac{1}{N})$ ,  $g$  is the random strength, and the entries of  $m$  and  $n$  are drawn from Gaussian  
 323 distributions  $m_i \sim \mathcal{N}(M_m, 1)$  and  $n_i \sim \mathcal{N}(M_n, 1)$ . We used EPI to infer the parameterizations of  
 324 rank-1 RNNs solving an example task, enabling discovery of properties of connectivity that result  
 325 in different types of error in the computation.

326 The task we consider is Gaussian posterior conditioning: calculate the parameters of a posterior  
 327 distribution induced by a prior  $p(\mu_y) = \mathcal{N}(\mu_0 = 4, \sigma_0^2 = 1)$  and a likelihood  $p(y|\mu_y) = \mathcal{N}(\mu_y, \sigma_y^2 =$   
 328 1), given a single observation  $y$ . Conjugacy offers the result analytically;  $p(\mu_y|y) = \mathcal{N}(\mu_{post}, \sigma_{post}^2)$ ,  
 329 where:

$$\mu_{post} = \frac{\frac{\mu_0}{\sigma_0^2} + \frac{y}{\sigma_y^2}}{\frac{1}{\sigma_0^2} + \frac{1}{\sigma_y^2}} \quad \sigma_{post}^2 = \frac{1}{\frac{1}{\sigma_0^2} + \frac{1}{\sigma_y^2}}. \quad (12)$$

330 The RNN is trained to solve this task by producing readout activity that is on average the posterior  
 331 mean  $\mu_{post}$ , and activity whose variability is the posterior variance  $\sigma_{post}^2$  (Fig. 5A, a setup inspired  
 332 by [51]). To solve this Gaussian posterior conditioning task, the RNN response to a constant input  
 333  $h = yw + (n - M_n)$  must equal the posterior mean along readout vector  $r$ , where

$$\kappa_r = \frac{1}{N} \sum_{j=1}^N r_j \phi(x_j) \quad (13)$$

334 Additionally, the amount of chaotic variance  $\Delta_T$  must equal the posterior variance. Theory for  
 335 low-rank RNNs allows us to express  $\kappa_r$  and  $\Delta_T$  in terms of each other through a solvable system  
 336 of nonlinear equations (see Section B.2.4) [26]. This allows us to mathematically formalize the  
 337 execution of this task into an emergent property, where the emergent property statistics of the  
 338 RNN activity are  $\kappa_r$  and  $\Delta_T$  and the emergent property values are the ground truth posterior  
 339 mean  $\mu_{post}$  and variance  $\sigma_{post}^2$ :

$$\mathbb{E} \begin{bmatrix} \kappa_r \\ \Delta_T \\ (\kappa_r - \mu_{post})^2 \\ (\Delta_T^2 - \sigma_{post}^2)^2 \end{bmatrix} = \begin{bmatrix} \mu_{post} \\ \sigma_{post}^2 \\ 0.1 \\ 0.1 \end{bmatrix} \quad (14)$$

340 We specify a substantial amount of variance in these emergent property statistics, so that the  
 341 inferred distribution results in RNNs with a variety errors in their solutions to the gaussian posterior  
 342 conditioning problem.

343 We used EPI to learn distributions of RNN connectivity properties  $z = [g \ M_m \ M_n]$  executing  
 344 Gaussian posterior conditioning given an input of  $y = 2$  (see Section B.2.4) (Fig. 5B). The true  
 345 Gaussian conditioning posterior for an input of  $y = 2$  is  $\mu_{\text{post}} = 3$  and  $\sigma_{\text{post}} = 0.5$ . We examined the  
 346 nature of the over- and under-estimation of the posterior means (Fig. 5B, left) and variances (Fig.  
 347 5B, right) in the inferred distributions. There is rough symmetry in the  $M_m$ - $M_n$  plane, suggesting  
 348 a degeneracy in the product of  $M_m$  and  $M_n$  (Fig. 5B). The product of  $M_m$  and  $M_n$  strongly  
 349 determines the posterior mean (Fig. 5B, left), and the random strength  $g$  is the most influential  
 350 variable on the chaotic variance (Fig. 5B, right). Neither of these observations were obvious from  
 351 what mathematical analysis is available in networks of this type (see Section B.2.4). While the  
 352 relationship of the random strength to chaotic variance (and resultingly posterior variance in this  
 353 problem) is well-known [3], the distribution admits a hypothesis: the estimation of the posterior  
 354 mean by the RNN increases with the product of  $M_m$  and  $M_n$ .

355 We tested this prediction by taking parameters  $z_1$  and  $z_2$  as representative samples from the positive  
 356 and negative  $M_m$ - $M_n$  quadrants, respectively. Instead of using the theoretical predictions shown  
 357 in Figure 5B, we simulated finite-size realizations of these networks with 2,000 neurons (e.g. Fig.  
 358 5C). We perturbed these parameter choices by the product  $M_m M_n$  clarifying that the posterior  
 359 mean can be directly controlled in this way (Fig. 5D). Thus, EPI confers a clear picture of error in  
 360 this computation: the product of the low rank vector means  $M_m$  and  $M_n$  modulates the estimated  
 361 posterior mean while the random strength  $g$  modulates the estimated posterior variance. This  
 362 novel procedure of inference on reduced parameterizations of RNNs conditioned on the emergent  
 363 property of task execution is generalizable to other settings modeled in [26] like noisy integration  
 364 and context-dependent decision making (Fig. S5).

## 365 4 Discussion

### 366 4.1 EPI is a general tool for theoretical neuroscience

367 Biologically realistic models of neural circuits are comprised of complex nonlinear differential equa-  
 368 tions, making traditional theoretical analysis and statistical inference intractable. In contrast, EPI  
 369 is capable of learning distributions of parameters in such models producing measurable signatures  
 370 of computation. We have demonstrated its utility on biological models (STG), intermediate-level  
 371 models of interacting genetically- and functionally-defined neuron-types (V1, SC), and the most  
 372 abstract of models (RNNs). We are able to condition both deterministic and stochastic models on

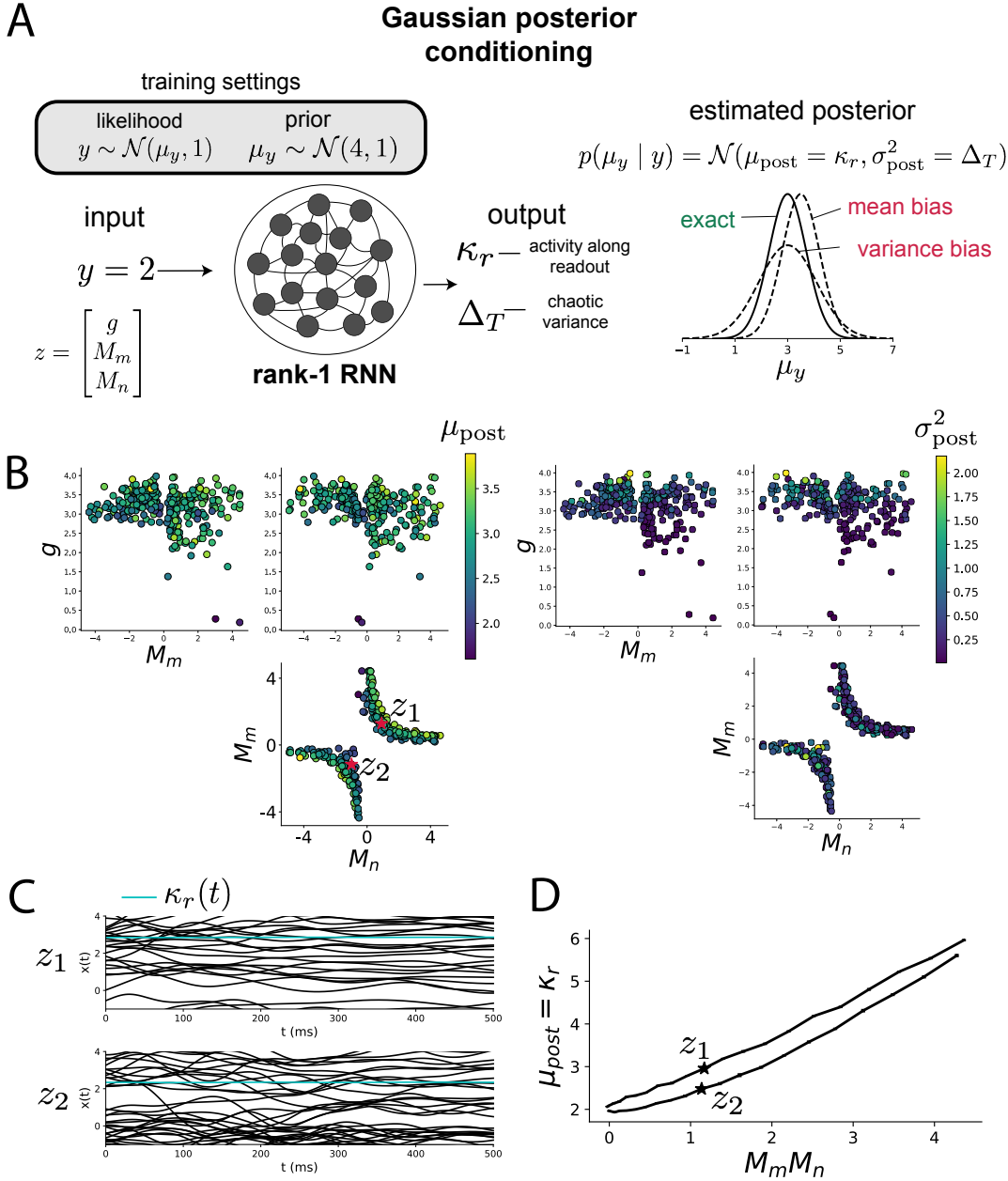


Figure 5: Sources of error in an RNN solving a simple task. A. (left) A rank-1 RNN executing a Gaussian posterior conditioning computation on  $\mu_y$ . (right) Error in this computation can come from over- or under-estimating the posterior mean or variance. B. EPI distribution of rank-1 RNNs executing Gaussian posterior conditioning. Samples are colored by (left) posterior mean  $\mu_{\text{post}} = \kappa_r$  and (right) posterior variance  $\sigma_{\text{post}}^2 = \Delta_T$ . C. Finite-size network simulations of 2,000 neurons with parameters  $z_1$  and  $z_2$  sampled from the inferred distribution. Activity along readout  $\kappa_r$  (cyan) is stable despite chaotic fluctuations. D. The posterior mean computed by RNNs parameterized by  $z_1$  and  $z_2$  pertrubed in the dimension of the product of  $M_m$  and  $M_n$ . Means and standard errors are shown across 10 realizations of 2,000-neuron networks.

373 low-level emergent properties like spiking frequency of membrane potentials, as well as high-level  
374 cognitive function like posterior conditioning. Technically, EPI is tractable when the emergent  
375 property statistics are continuously differentiable with respect to the model parameters, which is  
376 very often the case; this emphasizes the general applicability of EPI.

377 In this study, we have focused on applying EPI to low dimensional parameter spaces of models  
378 with low dimensional dynamical states. These choices were made to present the reader with a  
379 series of interpretable conclusions, which is more challenging in high dimensional spaces. In fact,  
380 EPI should scale reasonably to high dimensional parameter spaces, as the underlying technology has  
381 produced state-of-the-art performance on high-dimensional tasks such as texture generation [20]. Of  
382 course, increasing the dimensionality of the dynamical state of the model makes optimization more  
383 expensive, and there is a practical limit there as with any machine learning approach. Although,  
384 theoretical approaches (e.g. [26]) can be used to reason about the wholistic activity of such high  
385 dimensional systems by introducing some degree of additional structure into the model.

386 There are additional technical considerations when assessing the suitability of EPI for a particu-  
387 lar modeling question. First and foremost, as in any optimization problem, the defined emergent  
388 property should always be appropriately conditioned (constraints should not have wildly different  
389 units). Furthermore, if the program is underconstrained (not enough constraints), the distribution  
390 grows (in entropy) unstably unless mapped to a finite support. If overconstrained, there is no pa-  
391 rameter set producing the emergent property, and EPI optimization will fail (appropriately). Next,  
392 one should consider the computational cost of the gradient calculations. In the best circumstance,  
393 there is a simple, closed form expression (e.g. Section B.1.1) for the emergent property statistic  
394 given the model parameters. On the other end of the spectrum, many forward simulation iterations  
395 may be required before a high quality measurement of the emergent property statistic is available  
396 (e.g. Section B.2.1). In such cases, optimization will be expensive.

## 397 4.2 Novel hypotheses from EPI

398 In neuroscience, machine learning has primarily been used to revealed structure in large-scale neural  
399 datasets [52, 53, 54, 55, 56, 57] (see review, [15]). Such careful inference procedures are developed  
400 for these statistical models allowing precise, quantitative reasoning, which clarifies the way data  
401 informs knowledge of the model parameters. However, these inferable statistical models lack re-  
402 semblance to the underlying biology, making it unclear how to go from the structure revealed by  
403 these methods, to the neural mechanisms giving rise to it. In contrast, theoretical neuroscience has

404 focused on careful mechanistic modeling and the production of emergent properties of computation.  
405 The careful steps of 1.) model design and 2.) emergent property definition, are followed by 3.)  
406 practical inference methods resulting in an opaque characterization of the way model parameters  
407 govern computation. In this work, we replaced this opaque procedure of parameter identification  
408 in theoretical neuroscience with emergent property inference, opening the door to careful inference  
409 in careful models of neural computation.

410 Biologically realistic models of neural circuits often prove formidable to analyze. For example,  
411 consider the fact that we do not fully understand the (only) four-dimensional models of V1 [24]  
412 and SC [25]. Because analytical approaches to studying nonlinear dynamical systems become  
413 increasingly complicated when stepping from two-dimensional to three- or four-dimensional systems  
414 in the absence of restrictive simplifying assumptions [58], it is unsurprising that these models pose a  
415 challenge. In Section 3.3, we showed that EPI was far more informative about neuron-type input-  
416 responsivity than the predictions afforded through the available linear analytical methods. By  
417 flexibly conditioning this V1 model on different emergent properties, we performed an exploratory  
418 analysis of a *model* rather than a dataset, which generated a set of testable hypotheses, which  
419 were proved out. Of course, exploratory analyses can be directed towards formulating hypotheses  
420 of a specific form. For example, when interested in model parameter changes with behavioral  
421 performance, one can use EPI to condition on various levels of task accuracy as we did in Section  
422 3.4. This analysis identified experimentally testable predictions (proved out *in-silico*) of patterns  
423 of effective connectivity in SC that should be correlated with increased performance.

424 In our final analysis, we presented a novel procedure for doing statistical inference on interpretable  
425 parameterizations of RNNs executing simple tasks. Specifically, we analyzed RNNs solving a pos-  
426 terior conditioning problem in the spirit of [51]. This methodology relies on recently extended  
427 theory of responses in random neural networks with minimal structure [26]. While we focused on  
428 rank-1 RNNs, which were sufficient for solving this task, we can more generally use this approach  
429 to analyze rank-2 and greater RNNs. The ability to apply the probabilistic model selection toolkit  
430 to such black box models should prove invaluable as their use in neuroscience increases.

## 431 References

- 432 [1] Larry F Abbott. Theoretical neuroscience rising. *Neuron*, 60(3):489–495, 2008.

- 433 [2] John J Hopfield. Neural networks and physical systems with emergent collective computational  
434 abilities. *Proceedings of the national academy of sciences*, 79(8):2554–2558, 1982.
- 435 [3] Haim Sompolinsky, Andrea Crisanti, and Hans-Jurgen Sommers. Chaos in random neural  
436 networks. *Physical review letters*, 61(3):259, 1988.
- 437 [4] Misha V Tsodyks, William E Skaggs, Terrence J Sejnowski, and Bruce L McNaughton. Para-  
438 doxical effects of external modulation of inhibitory interneurons. *Journal of neuroscience*,  
439 17(11):4382–4388, 1997.
- 440 [5] Kong-Fatt Wong and Xiao-Jing Wang. A recurrent network mechanism of time integration in  
441 perceptual decisions. *Journal of Neuroscience*, 26(4):1314–1328, 2006.
- 442 [6] Diederik P Kingma and Max Welling. Auto-encoding variational bayes. *International Confer-  
443 ence on Learning Representations*, 2014.
- 444 [7] Danilo Jimenez Rezende, Shakir Mohamed, and Daan Wierstra. Stochastic backpropagation  
445 and variational inference in deep latent gaussian models. *International Conference on Machine  
446 Learning*, 2014.
- 447 [8] Yuanjun Gao, Evan W Archer, Liam Paninski, and John P Cunningham. Linear dynamical  
448 neural population models through nonlinear embeddings. In *Advances in neural information  
449 processing systems*, pages 163–171, 2016.
- 450 [9] Yuan Zhao and Il Memming Park. Recursive variational bayesian dual estimation for nonlinear  
451 dynamics and non-gaussian observations. *stat*, 1050:27, 2017.
- 452 [10] Gabriel Barello, Adam Charles, and Jonathan Pillow. Sparse-coding variational auto-encoders.  
453 *bioRxiv*, page 399246, 2018.
- 454 [11] Chethan Pandarinath, Daniel J O’Shea, Jasmine Collins, Rafal Jozefowicz, Sergey D Stavisky,  
455 Jonathan C Kao, Eric M Trautmann, Matthew T Kaufman, Stephen I Ryu, Leigh R Hochberg,  
456 et al. Inferring single-trial neural population dynamics using sequential auto-encoders. *Nature  
457 methods*, page 1, 2018.
- 458 [12] Alexander B Wiltschko, Matthew J Johnson, Giuliano Iurilli, Ralph E Peterson, Jesse M  
459 Katon, Stan L Pashkovski, Victoria E Abraira, Ryan P Adams, and Sandeep Robert Datta.  
460 Mapping sub-second structure in mouse behavior. *Neuron*, 88(6):1121–1135, 2015.

- [461] [13] Matthew J Johnson, David K Duvenaud, Alex Wiltschko, Ryan P Adams, and Sandeep R Datta. Composing graphical models with neural networks for structured representations and fast inference. In *Advances in neural information processing systems*, pages 2946–2954, 2016.
- [464] [14] Eleanor Batty, Matthew Whiteway, Shreya Saxena, Dan Biderman, Taiga Abe, Simon Musall, Winthrop Gillis, Jeffrey Markowitz, Anne Churchland, John Cunningham, et al. Behavenet: nonlinear embedding and bayesian neural decoding of behavioral videos. *Advances in Neural Information Processing Systems*, 2019.
- [468] [15] Liam Paninski and John P Cunningham. Neural data science: accelerating the experiment-analysis-theory cycle in large-scale neuroscience. *Current opinion in neurobiology*, 50:232–241, 2018.
- [471] [16] Mark K Transtrum, Benjamin B Machta, Kevin S Brown, Bryan C Daniels, Christopher R Myers, and James P Sethna. Perspective: Sloppiness and emergent theories in physics, biology, and beyond. *The Journal of chemical physics*, 143(1):07B201\_1, 2015.
- [474] [17] Danilo Jimenez Rezende and Shakir Mohamed. Variational inference with normalizing flows. *International Conference on Machine Learning*, 2015.
- [476] [18] Laurent Dinh, Jascha Sohl-Dickstein, and Samy Bengio. Density estimation using real nvp. *arXiv preprint arXiv:1605.08803*, 2016.
- [478] [19] George Papamakarios, Theo Pavlakou, and Iain Murray. Masked autoregressive flow for density estimation. In *Advances in Neural Information Processing Systems*, pages 2338–2347, 2017.
- [480] [20] Gabriel Loaiza-Ganem, Yuanjun Gao, and John P Cunningham. Maximum entropy flow networks. *International Conference on Learning Representations*, 2017.
- [482] [21] Dustin Tran, Rajesh Ranganath, and David Blei. Hierarchical implicit models and likelihood-free variational inference. In *Advances in Neural Information Processing Systems*, pages 5523–5533, 2017.
- [485] [22] Mark S Goldman, Jorge Golowasch, Eve Marder, and LF Abbott. Global structure, robustness, and modulation of neuronal models. *Journal of Neuroscience*, 21(14):5229–5238, 2001.
- [487] [23] Gabrielle J Gutierrez, Timothy O’Leary, and Eve Marder. Multiple mechanisms switch an electrically coupled, synaptically inhibited neuron between competing rhythmic oscillators. *Neuron*, 77(5):845–858, 2013.

- 490 [24] Ashok Litwin-Kumar, Robert Rosenbaum, and Brent Doiron. Inhibitory stabilization and vi-  
491       sual coding in cortical circuits with multiple interneuron subtypes. *Journal of neurophysiology*,  
492       115(3):1399–1409, 2016.
- 493 [25] Chunyu A Duan, Marino Pagan, Alex T Piet, Charles D Kopec, Athena Akrami, Alexander J  
494       Riordan, Jeffrey C Erlich, and Carlos D Brody. Collicular circuits for flexible sensorimotor  
495       routing. *bioRxiv*, page 245613, 2018.
- 496 [26] Francesca Mastrogiovanni and Srdjan Ostožić. Linking connectivity, dynamics, and computa-  
497       tions in low-rank recurrent neural networks. *Neuron*, 99(3):609–623, 2018.
- 498 [27] Sean R Bittner, Agostina Palmigiano, Kenneth D Miller, and John P Cunningham. Degener-  
499       ate solution networks for theoretical neuroscience. *Computational and Systems Neuroscience  
500       Meeting (COSYNE), Lisbon, Portugal*, 2019.
- 501 [28] Sean R Bittner, Alex T Piet, Chunyu A Duan, Agostina Palmigiano, Kenneth D Miller,  
502       Carlos D Brody, and John P Cunningham. Examining models in theoretical neuroscience with  
503       degenerate solution networks. *Bernstein Conference 2019, Berlin, Germany*, 2019.
- 504 [29] Marcel Nonnenmacher, Pedro J Goncalves, Giacomo Bassetto, Jan-Matthis Lueckmann, and  
505       Jakob H Macke. Robust statistical inference for simulation-based models in neuroscience. In  
506       *Bernstein Conference 2018, Berlin, Germany*, 2018.
- 507 [30] Deistler Michael, , Pedro J Goncalves, Kaan Oecal, and Jakob H Macke. Statistical inference for  
508       analyzing sloppiness in neuroscience models. In *Bernstein Conference 2019, Berlin, Germany*,  
509       2019.
- 510 [31] Jan-Matthis Lueckmann, Pedro J Goncalves, Giacomo Bassetto, Kaan Öcal, Marcel Nonnen-  
511       macher, and Jakob H Macke. Flexible statistical inference for mechanistic models of neural  
512       dynamics. In *Advances in Neural Information Processing Systems*, pages 1289–1299, 2017.
- 513 [32] Eve Marder and Vatsala Thirumalai. Cellular, synaptic and network effects of neuromodula-  
514       tion. *Neural Networks*, 15(4-6):479–493, 2002.
- 515 [33] Astrid A Prinz, Dirk Bucher, and Eve Marder. Similar network activity from disparate circuit  
516       parameters. *Nature neuroscience*, 7(12):1345, 2004.
- 517 [34] Edwin T Jaynes. Information theory and statistical mechanics. *Physical review*, 106(4):620,  
518       1957.

- 519 [35] Gamaleldin F Elsayed and John P Cunningham. Structure in neural population recordings:  
520 an expected byproduct of simpler phenomena? *Nature neuroscience*, 20(9):1310, 2017.
- 521 [36] Cristina Savin and Gašper Tkačik. Maximum entropy models as a tool for building precise  
522 neural controls. *Current opinion in neurobiology*, 46:120–126, 2017.
- 523 [37] Brendan K Murphy and Kenneth D Miller. Balanced amplification: a new mechanism of  
524 selective amplification of neural activity patterns. *Neuron*, 61(4):635–648, 2009.
- 525 [38] Hirofumi Ozeki, Ian M Finn, Evan S Schaffer, Kenneth D Miller, and David Ferster. Inhibitory  
526 stabilization of the cortical network underlies visual surround suppression. *Neuron*, 62(4):578–  
527 592, 2009.
- 528 [39] Daniel B Rubin, Stephen D Van Hooser, and Kenneth D Miller. The stabilized supralinear  
529 network: a unifying circuit motif underlying multi-input integration in sensory cortex. *Neuron*,  
530 85(2):402–417, 2015.
- 531 [40] Henry Markram, Maria Toledo-Rodriguez, Yun Wang, Anirudh Gupta, Gilad Silberberg, and  
532 Caizhi Wu. Interneurons of the neocortical inhibitory system. *Nature reviews neuroscience*,  
533 5(10):793, 2004.
- 534 [41] Bernardo Rudy, Gordon Fishell, Soohyun Lee, and Jens Hjerling-Leffler. Three groups of  
535 interneurons account for nearly 100% of neocortical gabaergic neurons. *Developmental neuro-*  
536 *biology*, 71(1):45–61, 2011.
- 537 [42] Robin Tremblay, Soohyun Lee, and Bernardo Rudy. GABAergic Interneurons in the Neocortex:  
538 From Cellular Properties to Circuits. *Neuron*, 91(2):260–292, 2016.
- 539 [43] Carsten K Pfeffer, Mingshan Xue, Miao He, Z Josh Huang, and Massimo Scanziani. Inhi-  
540 bition of inhibition in visual cortex: the logic of connections between molecularly distinct  
541 interneurons. *Nature Neuroscience*, 16(8):1068, 2013.
- 542 [44] Luis Carlos Garcia Del Molino, Guangyu Robert Yang, Jorge F. Mejias, and Xiao Jing Wang.  
543 Paradoxical response reversal of top- down modulation in cortical circuits with three interneu-  
544 ron types. *Elife*, 6:1–15, 2017.
- 545 [45] Guang Chen, Carl Van Vreeswijk, David Hansel, and David Hansel. Mechanisms underlying  
546 the response of mouse cortical networks to optogenetic manipulation. 2019.

- 547 [46] (2018) Allen Institute for Brain Science. Layer 4 model of v1. available from:  
548 <https://portal.brain-map.org/explore/models/l4-mv1>.
- 549 [47] Yazan N Billeh, Binghuang Cai, Sergey L Gratiy, Kael Dai, Ramakrishnan Iyer, Nathan W  
550 Gouwens, Reza Abbasi-Asl, Xiaoxuan Jia, Joshua H Siegle, Shawn R Olsen, et al. Systematic  
551 integration of structural and functional data into multi-scale models of mouse primary visual  
552 cortex. *bioRxiv*, page 662189, 2019.
- 553 [48] Chunyu A Duan, Jeffrey C Erlich, and Carlos D Brody. Requirement of prefrontal and midbrain  
554 regions for rapid executive control of behavior in the rat. *Neuron*, 86(6):1491–1503, 2015.
- 555 [49] Omri Barak. Recurrent neural networks as versatile tools of neuroscience research. *Current  
556 opinion in neurobiology*, 46:1–6, 2017.
- 557 [50] David Sussillo and Omri Barak. Opening the black box: low-dimensional dynamics in high-  
558 dimensional recurrent neural networks. *Neural computation*, 25(3):626–649, 2013.
- 559 [51] Rodrigo Echeveste, Laurence Aitchison, Guillaume Hennequin, and Máté Lengyel. Cortical-like  
560 dynamics in recurrent circuits optimized for sampling-based probabilistic inference. *bioRxiv*,  
561 page 696088, 2019.
- 562 [52] Robert E Kass and Valérie Ventura. A spike-train probability model. *Neural computation*,  
563 13(8):1713–1720, 2001.
- 564 [53] Emery N Brown, Loren M Frank, Dengda Tang, Michael C Quirk, and Matthew A Wilson.  
565 A statistical paradigm for neural spike train decoding applied to position prediction from  
566 ensemble firing patterns of rat hippocampal place cells. *Journal of Neuroscience*, 18(18):7411–  
567 7425, 1998.
- 568 [54] Liam Paninski. Maximum likelihood estimation of cascade point-process neural encoding  
569 models. *Network: Computation in Neural Systems*, 15(4):243–262, 2004.
- 570 [55] M Yu Byron, John P Cunningham, Gopal Santhanam, Stephen I Ryu, Krishna V Shenoy, and  
571 Maneesh Sahani. Gaussian-process factor analysis for low-dimensional single-trial analysis  
572 of neural population activity. In *Advances in neural information processing systems*, pages  
573 1881–1888, 2009.

- 574 [56] Kenneth W Latimer, Jacob L Yates, Miriam LR Meister, Alexander C Huk, and Jonathan W  
 575 Pillow. Single-trial spike trains in parietal cortex reveal discrete steps during decision-making.  
 576 *Science*, 349(6244):184–187, 2015.
- 577 [57] Lea Duncker, Gergo Bohner, Julien Boussard, and Maneesh Sahani. Learning interpretable  
 578 continuous-time models of latent stochastic dynamical systems. *Proceedings of the 36th Inter-*  
 579 *national Conference on Machine Learning*, 2019.
- 580 [58] Steven H Strogatz. Nonlinear dynamics and chaos: with applications to physics. *Biology,*  
 581 *Chemistry, and Engineering (Studies in Nonlinearity)*, Perseus, Cambridge, UK, 1994.
- 582 [59] Rajesh Ranganath, Sean Gerrish, and David Blei. Black box variational inference. In *Artificial*  
 583 *Intelligence and Statistics*, pages 814–822, 2014.
- 584 [60] Martin J Wainwright, Michael I Jordan, et al. Graphical models, exponential families, and  
 585 variational inference. *Foundations and Trends® in Machine Learning*, 1(1–2):1–305, 2008.
- 586 [61] Diederik P Kingma and Jimmy Ba. Adam: A method for stochastic optimization. *International*  
 587 *Conference on Learning Representations*, 2015.
- 588 [62] Laurent Dinh, Jascha Sohl-Dickstein, and Samy Bengio. Density estimation using real nvp.  
 589 *Proceedings of the 5th International Conference on Learning Representations*, 2017.
- 590 [63] David M Blei, Alp Kucukelbir, and Jon D McAuliffe. Variational inference: A review for  
 591 statisticians. *Journal of the American Statistical Association*, 112(518):859–877, 2017.

592 **A Acknowledgements**

593 This work was funded by NSF Graduate Research Fellowship, DGE-1644869, McKnight Endow-  
 594 ment Fund, NIH NINDS 5R01NS100066, Simons Foundation 542963, NSF NeuroNex Award DBI-  
 595 1707398, and The Gatsby Charitable Foundation. Helpful conversations were had with Francesca  
 596 Mastrogiovisepppe, Srdjan Ostojic, James Fitzgerald, Stephen Baccus, Dhruva Raman, Mehrdad  
 597 Jazayeri, Liam Paninski, and Larry Abbott.

598 **B Methods**

599 **B.1 Emergent property inference (EPI)**

600 Emergent property inference (EPI) learns distributions of theoretical model parameters that pro-  
 601 duce emergent properties of interest by combining ideas from maximum entropy flow networks  
 602 (MEFNs) [20] and likelihood-free variational inference (LFVI) [21]. Consider model parameteri-  
 603 zation  $z$  and data  $x$  which has an intractable likelihood  $p(x | z)$  defined by a model simulator of  
 604 which samples are available  $x \sim p(x | z)$ . EPI optimizes a distribution  $q_\theta(z)$  (itself parameterized  
 605 by  $\theta$ ) of model parameters  $z$  to produce an emergent property of interest  $\mathcal{B}$ ,

$$\mathcal{B} \triangleq \mathbb{E}_{z \sim q_\theta} [\mathbb{E}_{x \sim p(x|z)} [T(x)]] = \mu \quad (15)$$

606 Precisely, over the EPI distribution of parameters  $q_\theta(z)$  and distribution of simulated activity  
 607  $p(x | z)$ , the emergent property statistics  $T(x)$  must equal the emergent property values  $\mu$  on  
 608 average. This is a viable way to represent emergent properties in theoretical models, as we have  
 609 demonstrated in the main text, and enables the EPI optimization.

610 With EPI, we use deep probability distributions to learn flexible approximations to model parameter  
 611 distributions  $q_\theta(z)$ . In deep probability distributions, a simple random variable  $w \sim q_0(w)$  is  
 612 mapped deterministically via a sequence of deep neural network layers ( $f_1, \dots, f_l$ ) parameterized by  
 613 weights and biases  $\theta$  to the support of the distribution of interest:

$$z = f_\theta(\omega) = f_l(\dots f_1(w)) \quad (16)$$

614 Given a simulator defined by a theoretical model  $x \sim p(x | z)$  and some emergent property of  
 615 interest  $\mathcal{B}$ ,  $q_\theta(z)$  is optimized via the neural network parameters  $\theta$  to find an optimally entropic  
 616 distribution  $q_\theta^*$  within the deep variational family  $\mathcal{Q}$  producing the emergent property:

$$q_\theta^*(z) = \underset{q_\theta \in \mathcal{Q}}{\operatorname{argmax}} H(q_\theta(z)) \quad (17)$$

s.t.  $\mathbb{E}_{z \sim q_\theta} [\mathbb{E}_{x \sim p(x|z)} [T(x)]] = \mu$

617 Since we are optimizing parameters  $\theta$  of our deep probability distribution with respect to the entropy  
 618  $H(q_\theta(z))$ , we will need to take gradients with respect to the log probability density of samples from  
 619 the deep probability distribution.

$$H(q_\theta(z)) = \int -q_\theta(z) \log(q_\theta(z)) dz = \mathbb{E}_{z \sim q_\theta} [-\log(q_\theta(z))] = \mathbb{E}_{w \sim q_0} [-\log(q_\theta(f_\theta(w)))] \quad (18)$$

$$\nabla_\theta H(q_\theta(z)) = \mathbb{E}_{w \sim q_0} [-\nabla_\theta \log(q_\theta(f_\theta(w)))] \quad (19)$$

621 This optimization is done using the approach of MEFN [20], using architectures for deep probability  
 622 distributions, called normalizing flows (see Section B.1.3), conferring a tractable calculation of  
 623 sample log probability. In EPI, this methodology for learning maximum entropy distributions is  
 624 repurposed toward variational learning of model parameter distributions. Similar to LFVI [21], we  
 625 are motivated to do variational learning in models with intractable likelihood functions, in which  
 626 standard methods like stochastic gradient variational Bayes [6] or black box variational inference[59]  
 627 are not tractable. Furthermore, EPI focuses on setting mathematically defined emergent property  
 628 statistics to emergent property values of interest, whereas LFVI is focused on learning directly from  
 629 datasets. Optimizing this objective is a technological challenge, the details of which we elaborate  
 630 in Section B.1.2. Before going through those details, we ground this optimization in a toy example.

### 631 B.1.1 Example: 2D LDS

632 To gain intuition for EPI, consider a two-dimensional linear dynamical system model:

$$\tau \frac{dx}{dt} = Ax \quad (20)$$

633 with

$$A = \begin{bmatrix} a_1 & a_2 \\ a_3 & a_4 \end{bmatrix} \quad (21)$$

634 To run EPI with the dynamics matrix elements as the free parameters  $z = [a_1 \ a_2 \ a_3 \ a_4]$  (fixing  
 635  $\tau = 1$ ), the emergent property statistics  $T(x)$  were chosen to contain the first- and second-moments  
 636 of the oscillatory frequency  $2\pi\text{imag}(\lambda_1)$  and the growth/decay factor  $\text{real}(\lambda_1)$  of the oscillating  
 637 system.  $\lambda_1$  is the eigenvalue of greatest real part when the imaginary component is zero, and  
 638 alternatively of positive imaginary component when the eigenvalues are complex conjugate pairs.  
 639 To learn the distribution of real entries of  $A$  that produce a band of oscillating systems around  
 640 1Hz, we formalized this emergent property as  $\text{real}(\lambda_1)$  having mean zero with variance  $0.25^2$ , and  
 641 the oscillation frequency  $2\pi\text{imag}(\lambda_1)$  having mean  $\omega = 1$  Hz with variance  $(0.1\text{Hz})^2$ :

$$\mathbb{E}[T(x)] \triangleq \mathbb{E} \begin{bmatrix} \text{real}(\lambda_1) \\ \text{imag}(\lambda_1) \\ (\text{real}(\lambda_1) - 0)^2 \\ (\text{imag}(\lambda_1) - 2\pi\omega)^2 \end{bmatrix} = \begin{bmatrix} 0.0 \\ 2\pi\omega \\ 0.25^2 \\ (2\pi 0.1)^2 \end{bmatrix} \triangleq \mu \quad (22)$$

642

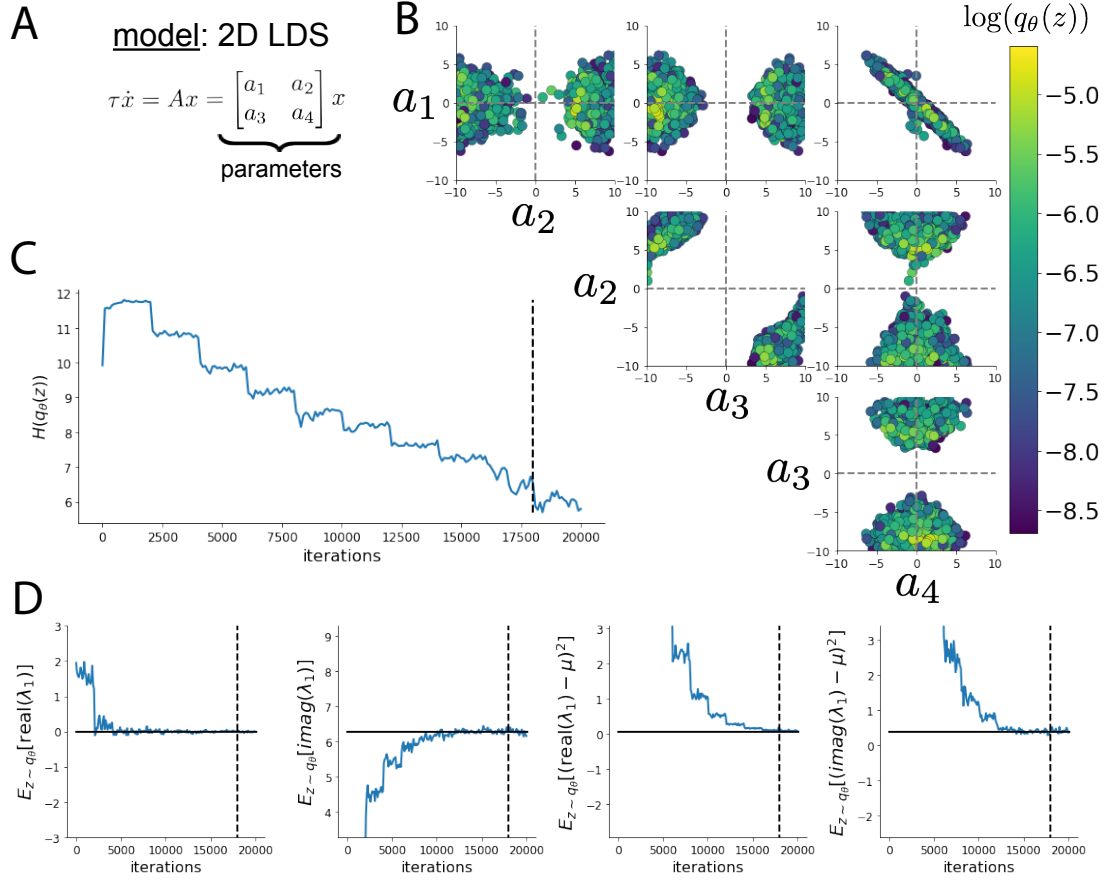


Fig. S1: A. Two-dimensional linear dynamical system model, where real entries of the dynamics matrix  $A$  are the parameters. B. The DSN distribution for a two-dimensional linear dynamical system with  $\tau = 1$  that produces an average of 1Hz oscillations with some small amount of variance. C. Entropy throughout the optimization. At the beginning of each augmented Lagrangian epoch (2,000 iterations), the entropy dipped due to the shifted optimization manifold where emergent property constraint satisfaction is increasingly weighted. D. Emergent property moments throughout optimization. At the beginning of each augmented Lagrangian epoch, the emergent property moments adjust closer to their constraints.

643 Unlike the models we presented in the main text, this model admits an analytical form for the the  
 644 mean emergent property statistics given parameter  $z$ , since the eigenvalues can be calculated using  
 645 the quadratic formula:

$$\lambda = \frac{\left(\frac{a_1+a_4}{\tau}\right) \pm \sqrt{\left(\frac{a_1+a_4}{\tau}\right)^2 + 4\left(\frac{a_2a_3-a_1a_4}{\tau}\right)}}{2} \quad (23)$$

646 Importantly, even though  $\mathbb{E}_{x \sim p(x|z)} [T(x)]$  is calculable directly via a closed form function and does  
 647 not require simulation, we cannot derive the distribution  $q_\theta^*$  directly. This is due to the formally hard  
 648 problem of the backward mapping: finding the natural parameters  $\eta$  from the mean parameters  $\mu$   
 649 of an exponential family distribution [60]. Instead, we used EPI to approximate this distribution  
 650 (Fig. S1B). We used a real-NVP normalizing flow architecture with four masks, two neural network  
 651 layers of 15 units per mask, with batch normalization momentum 0.99, mapped onto a support of  
 652  $z_i \in [-20, 20]$ . (see Section B.1.3).

653 Even this relatively simple system has nontrivial (though intuitively sensible) structure in the  
 654 parameter distribution. To validate our method (further than that of the underlying technology on  
 655 a ground truth solution [20]) we analytically derived the contours of the probability density from the  
 656 emergent property statistics and values (Fig. S2). In the  $a_1 - a_4$  plane, the black line at  $\text{real}(\lambda_1) =$   
 657  $\frac{a_1+a_4}{2} = 0$ , and the dotted black line at the standard deviation  $\text{real}(\lambda_1) = \frac{a_1+a_4}{2} \pm 0.25$ , and the gray  
 658 line at twice the standard deviation  $\text{real}(\lambda_1) = \frac{a_1+a_4}{2} \pm 0.5$  follow the contour of probability density  
 659 of the samples. (Fig. 2A). The distribution precisely reflects the desired statistical constraints and  
 660 model degeneracy in the sum of  $a_1$  and  $a_4$ . Intuitively, the parameters equivalent with respect to  
 661 emergent property statistic  $\text{real}(\lambda_1)$  have similar log densities.

662 To explain the bimodality of the EPI distribution, we examined the imaginary component of  $\lambda_1$ .  
 663 When  $\text{real}(\lambda_1) = \frac{a_1+a_4}{2} = 0$ , we have

$$\text{imag}(\lambda_1) = \begin{cases} \sqrt{\frac{a_1a_4-a_2a_3}{\tau}}, & \text{if } a_1a_4 < a_2a_3 \\ 0 & \text{otherwise} \end{cases} \quad (24)$$

664 When  $\tau = 1$  and  $a_1a_4 > a_2a_3$  (center of distribution above), we have the following equation for the  
 665 other two dimensions:

$$\text{imag}(\lambda_1)^2 = a_1a_4 - a_2a_3 \quad (25)$$

666 Since we constrained  $\mathbb{E}_{z \sim q_\theta} [\text{imag}(\lambda)] = 2\pi$  (with  $\omega = 1$ ), we can plot contours of the equation  
 667  $\text{imag}(\lambda_1)^2 = a_1a_4 - a_2a_3 = (2\pi)^2$  for various  $a_1a_4$  (Fig. S2A). If  $\sigma_{1,4} = \mathbb{E}_{z \sim q_\theta} (|a_1a_4 - E_{q_\theta}[a_1a_4]|)$ ,  
 668 then we plot the contours as  $a_1a_4 = 0$  (black),  $a_1a_4 = -\sigma_{1,4}$  (black dotted), and  $a_1a_4 = -2\sigma_{1,4}$

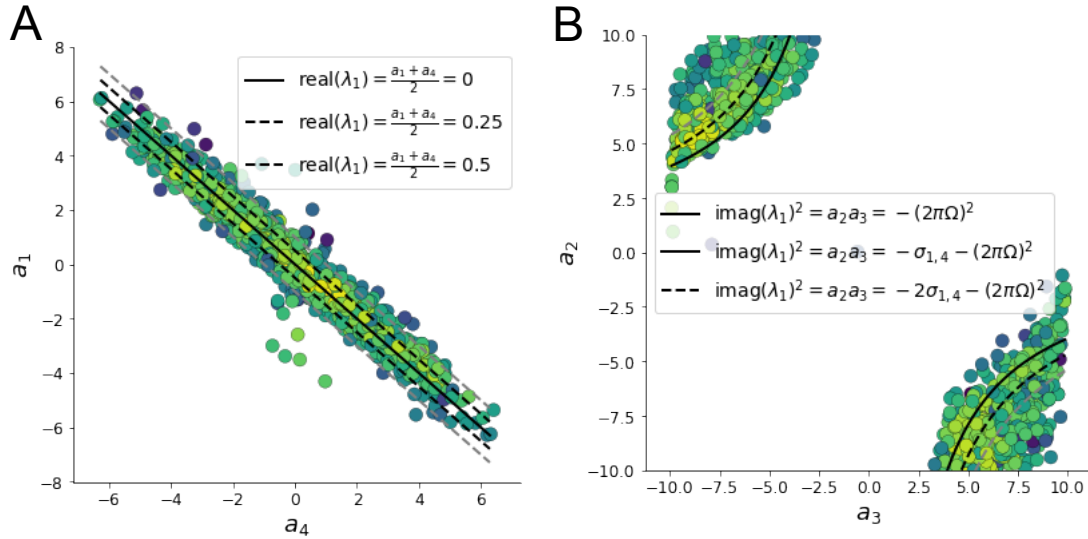


Fig. S2: A. Probability contours in the  $a_1 - a_4$  plane can be derived from the relationship to emergent property statistic of growth/decay factor  $\text{real}(\lambda_1)$ . B. Probability contours in the  $a_2 - a_3$  plane can be derived from the emergent property statistic of oscillation frequency  $2\pi\text{imag}(\lambda_1)$  (see text).

669 (grey dotted) (Fig. S2B). This validates the curved structure of the inferred distribution learned  
 670 through EPI. We take steps in negative standard deviation of  $a_1 a_4$  (dotted and gray lines), since  
 671 there are few positive values  $a_1 a_4$  in the learned distribution. Subtler combinations of model and  
 672 emergent property will have more complexity, further motivating the use of EPI for understanding  
 673 these systems. As we expect, the distribution results in samples of two-dimensional linear systems  
 674 oscillating near 1Hz (Fig. S3).

### 675 B.1.2 Augmented Lagrangian optimization

676 To optimize  $q_\theta(z)$  in Equation 17, the constrained optimization is executed using the augmented  
 677 Lagrangian method. The following objective is minimized:

$$L(\theta; \eta, c) = -H(q_\theta) + \eta^\top R(\theta) + \frac{c}{2} \|R(\theta)\|^2 \quad (26)$$

678 where  $R(\theta) = \mathbb{E}_{z \sim q_\theta} [\mathbb{E}_{x \sim p(x|z)} [T(x) - \mu]]$ ,  $\eta \in \mathbb{R}^m$  are the Lagrange multipliers where  $m = |\mu| = |T(x)|$ , and  $c$  is the penalty coefficient. These Lagrange multipliers are closely related to the natural  
 679 parameters of exponential families (see Section B.1.4). Deep neural network weights and biases  $\theta$  of  
 680 the deep probability distribution are optimized according to Equation 26 using the Adam optimizer  
 681

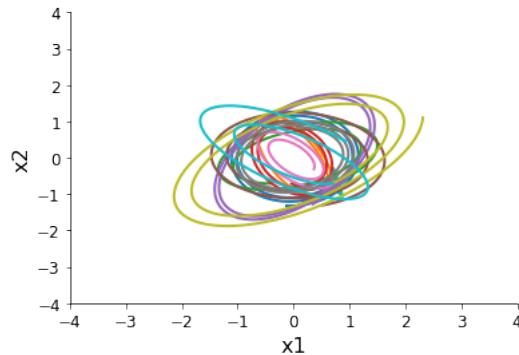


Fig. S3: Sampled dynamical system trajectories from the EPI distribution. Each trajectory is initialized at  $x(0) = \begin{bmatrix} \frac{\sqrt{2}}{2} & -\frac{\sqrt{2}}{2} \end{bmatrix}$ .

with its standard parameterization [61].  $\eta$  is initialized to the zero vector and adapted following each augmented Lagrangian epoch, which is a period of optimization with fixed  $(\eta, c)$  for a given number of stochastic optimization iterations. A low value of  $c$  is used initially, and conditionally increased after each epoch based on constraint error reduction. For example, the initial value of  $c$  was  $c_0 = 10^{-3}$  during EPI with the linear two-dimensional system (Fig. S1C). The penalty coefficient is updated based on the result of a hypothesis test regarding the reduction in constraint violation. The p-value of  $\mathbb{E}[||R(\theta_{k+1})||] > \gamma \mathbb{E}[||R(\theta_k)||]$  is computed, and  $c_{k+1}$  is updated to  $\beta c_k$  with probability  $1 - p$ . The other update rule is  $\eta_{k+1} = \eta_k + c_k \frac{1}{n} \sum_{i=1}^n (T(x^{(i)}) - \mu)$  given a batch size  $n$ . Throughout the study,  $\beta = 4.0$ ,  $\gamma = 0.25$ , and the batch size was a hyperparameter, which varied according to the application of EPI.

The intention is that  $c$  and  $\eta$  start at values encouraging entropic growth early in optimization. Then, as they increase in magnitude with each training epoch, the constraint satisfaction terms are increasingly weighted, resulting in a decrease in entropy. This encourages the discovery of suitable regions of parameter space, and the subsequent refinement of the distribution to produce the emergent property. In the two-dimensional example, each augmented Lagrangian epoch ran for 2,000 iterations (Fig. S1C-D). Notice the initial entropic growth, and subsequent reduction upon each update of  $\eta$  and  $c$ . The momentum parameters of the Adam optimizer were reset at the end of each augmented Lagrangian epoch.

Rather than starting optimization from some drawn  $\theta$  from a glorot uniform or other distribution, we found that initializing  $q_\theta(z)$  to approximate an isotropic Gaussian distribution conferred more stable, consistent optimization. The parameters of the initialization Gaussian were chosen

703 on an application-specific basis. Throughout the study, we chose isotropic Gaussians with mean  
 704  $\mu_{\text{init}}$  at the center of the distribution support and some standard deviation  $\sigma_{\text{init}}$ , except when we  
 705 demonstrate how to use grid search to inform the initialization in Section B.2.2.

706 To assess whether EPI distribution  $q_\theta(z)$  produces the emergent property, we defined a hypothesis  
 707 testing convergence criteria. The algorithm has converged when a null hypothesis test of constraint  
 708 violations  $R(\theta)_i$  being zero is accepted for all constraints  $i \in \{1, \dots, m\}$  at a significance threshold  
 709  $\alpha = 0.05$ . This significance threshold is adjusted through Bonferroni correction according to the  
 710 number of constraints  $m$ . The p-values for each constraint are calculated according to a two-  
 711 tailed nonparameteric test, where 200 estimations of the sample mean  $R(\theta)^i$  are made from  $k$   
 712 resamplings of  $z$  of a finite sample of size  $n$  taken at the end of the augmented Lagrangian epoch.  
 713  $k$  is determined by a fraction of the batch size  $\nu$ , which varies according to the application. In the  
 714 linear two-dimensional system example, we used a batch size of  $n = 1000$  and set  $\nu = 0.1$  resulting  
 715 in convergence after the ninth epoch of optimization. (Fig. S1C-D black dotted line).

### 716 B.1.3 Normalizing flows

717 Deep probability models typically consist of several layers of fully connected neural networks.  
 718 When each neural network layer is restricted to be a bijective function, the sample density can be  
 719 calculated using the change of variables formula at each layer of the network. For  $z' = f(z)$ ,

$$q(z') = q(f^{-1}(z')) \left| \det \frac{\partial f^{-1}(z')}{\partial z'} \right| = q(z) \left| \det \frac{\partial f(z)}{\partial z} \right|^{-1} \quad (27)$$

720 However, this computation has cubic complexity in dimensionality for fully connected layers. By  
 721 restricting our layers to normalizing flows [17] – bijective functions with fast log determinant Ja-  
 722 cobian computations, we can tractably optimize deep generative models with objectives that are a  
 723 function of sample density, like entropy. Most of our analyses use either a planar flow [17] or real  
 724 NVP [62], which have proven effective in our architecture searches. Planar flow architectures are  
 725 specified by the number of planar bijection layers used, while real NVP architectures are specified  
 726 by the number of masks, neural network layers per mask, units per layer, and batch normalization  
 727 momentum parameter.

728 **B.1.4 Emergent property inference as variational inference in an exponential family**

729 Consider the goal of doing variational inference with an exponential family posterior distribution  
 730  $p(z | x)$ . We use the following abbreviated notation to collect the base measure  $b(z)$  and sufficient  
 731 statistics  $T(z)$  into  $\tilde{T}(z)$  and likewise concatenate a 1 onto the end of the natural parameter  $\tilde{\eta}(x)$ .  
 732 The log normalizing constant  $A(\eta(x))$  remains unchanged.

$$\begin{aligned} p(z | x) &= b(z) \exp \left( \eta(x)^\top T(z) - A(\eta(x)) \right) = \exp \left( \begin{bmatrix} \eta(x) \\ 1 \end{bmatrix}^\top \begin{bmatrix} T(z) \\ b(z) \end{bmatrix} - A(\eta(x)) \right) \\ &= \exp \left( \tilde{\eta}(x)^\top \tilde{T}(z) - A(\eta(x)) \right) \end{aligned} \quad (28)$$

733 Variational inference with an exponential family posterior distribution uses optimization to mini-  
 734 mize the following divergence [63]:

$$q_\theta^* = \underset{q_\theta \in Q}{\operatorname{argmin}} KL(q_\theta || p(z | x)) \quad (29)$$

735  $q_\theta(z)$  is the variational approximation to the posterior with variational parameters  $\theta$ . We can write  
 736 this KL divergence in terms of entropy of the variational approximation.

$$KL(q_\theta || p(z | x)) = \mathbb{E}_{z \sim q_\theta} [\log(q_\theta(z))] - \mathbb{E}_{z \sim q_\theta} [\log(p(z | x))] \quad (30)$$

$$= -H(q_\theta) - \mathbb{E}_{z \sim q_\theta} [\tilde{\eta}(x)^\top \tilde{T}(z) - A(\eta(x))] \quad (31)$$

737 738 As far as the variational optimization is concerned, the log normalizing constant is independent of  
 739  $q_\theta(z)$ , so it can be dropped.

$$\underset{q_\theta \in Q}{\operatorname{argmin}} KL(q_\theta || p(z | x)) = \underset{q_\theta \in Q}{\operatorname{argmin}} -H(q_\theta) - \mathbb{E}_{z \sim q_\theta} [\tilde{\eta}(x)^\top \tilde{T}(z)] \quad (32)$$

740 Further, we can write the objective in terms of the first moment of the sufficient statistics  $\mu =$   
 741  $\mathbb{E}_{z \sim p(z|x)} [T(z)]$ .

$$= \underset{q_\theta \in Q}{\operatorname{argmin}} -H(q_\theta) - \mathbb{E}_{z \sim q_\theta} [\tilde{\eta}(x)^\top (\tilde{T}(z) - \mu)] + \tilde{\eta}(x)^\top \mu \quad (33)$$

$$= \underset{q_\theta \in Q}{\operatorname{argmin}} -H(q_\theta) - \mathbb{E}_{z \sim q_\theta} [\tilde{\eta}(x)^\top (\tilde{T}(z) - \mu)] \quad (34)$$

742 743 In comparison, in emergent property inference (EPI), we're solving the following problem.

$$q_\theta^*(z) = \underset{q_\theta \in Q}{\operatorname{argmax}} H(q_\theta(z)), \text{ s.t. } \mathbb{E}_{z \sim q_\theta} [\mathbb{E}_{x \sim p(x|z)} [T(x)]] = \mu \quad (35)$$

744 The Lagrangian objective (without the augmentation) is

$$q_\theta^* = \underset{q_\theta \in Q}{\operatorname{argmin}} -H(q_\theta) + \eta_{\text{opt}}^\top (\mathbb{E}_{z \sim q_\theta} [\tilde{T}(z)] - \mu) \quad (36)$$

745 As the optimization proceeds,  $\eta_{\text{opt}}^\top$  should converge to the natural parameter  $\tilde{\eta}(x)$  through its  
 746 adaptations in each epoch (see Section B.1.2).

747 The derivation of the natural parameter  $\tilde{\eta}(x)$  of an exponential family distribution from its mean  
 748 parameter  $\mu$  is referred to as the backward mapping and is formally hard to identify [60]. Since  
 749 this backward mapping is deterministic, we can replace the notation of  $p(z \mid x)$  with  $p(z \mid \mathcal{B})$   
 750 conceptualizing an inferred distribution that obeys emergent property  $\mathcal{B}$  (see Section B.1).

751 **B.2 Theoretical models**

752 In this study, we used emergent property inference to examine several models relevant to theoretical  
 753 neuroscience. Here, we provide the details of each model and the related analyses.

754 **B.2.1 Stomatogastric ganglion**

755 We analyze how the parameters  $z = [g_{el} \ g_{synA}]$  govern the emergent phenomena of network  
 756 syncing in a model of the stomatogastric ganglion (STG) shown in Figure 1A with activity  $x =$   
 757  $[x_{f1}, x_{f2}, x_{\text{hub}}, x_{s1}, x_{s2}]$ . Each neuron’s membrane potential  $x_\alpha(t)$  for  $\alpha \in \{f1, f2, \text{hub}, s1, s2\}$  is the  
 758 solution of the following differential equation:

$$C_m \frac{dx_\alpha}{dt} = -[h_{leak}(x; z) + h_{Ca}(x; z) + h_K(x; z) + h_{hyp}(x; z) + h_{elec}(x; z) + h_{syn}(x; z)] \quad (37)$$

759 The membrane potential of each neuron is affected by the leak, calcium, potassium, hyperpolariza-  
 760 tion, electrical and synaptic currents, respectively, which are functions of all membrane potentials  
 761 and the conductance parameters  $z$ . The capacitance of the cell membrane was set to  $C_m = 1nF$ .  
 762 Specifically, the currents are the difference in the neuron’s membrane potential and that current  
 763 type’s reversal potential multiplied by a conductance:

$$h_{leak}(x; z) = g_{leak}(x_\alpha - V_{leak}) \quad (38)$$

$$h_{elec}(x; z) = g_{el}(x_\alpha^{post} - x_\alpha^{pre}) \quad (39)$$

$$h_{syn}(x; z) = g_{syn}S_\infty^{pre}(x_\alpha^{post} - V_{syn}) \quad (40)$$

$$h_{Ca}(x; z) = g_{Ca}M_\infty(x_\alpha - V_{Ca}) \quad (41)$$

$$h_K(x; z) = g_KN(x_\alpha - V_K) \quad (42)$$

$$h_{hyp}(x; z) = g_hH(x_\alpha - V_{hyp}) \quad (43)$$

769 The reversal potentials were set to  $V_{leak} = -40mV$ ,  $V_{Ca} = 100mV$ ,  $V_K = -80mV$ ,  $V_{hyp} = -20mV$ ,  
 770 and  $V_{syn} = -75mV$ . The other conductance parameters were fixed to  $g_{leak} = 1 \times 10^{-4}\mu S$ .  $g_{Ca}$ ,  
 771  $g_K$ , and  $g_{hyp}$  had different values based on fast, intermediate (hub) or slow neuron. Fast:  $g_{Ca} =$   
 772  $1.9 \times 10^{-2}$ ,  $g_K = 3.9 \times 10^{-2}$ , and  $g_{hyp} = 2.5 \times 10^{-2}$ . Intermediate:  $g_{Ca} = 1.7 \times 10^{-2}$ ,  $g_K = 1.9 \times 10^{-2}$ ,  
 773 and  $g_{hyp} = 8.0 \times 10^{-3}$ . Intermediate:  $g_{Ca} = 8.5 \times 10^{-3}$ ,  $g_K = 1.5 \times 10^{-2}$ , and  $g_{hyp} = 1.0 \times 10^{-2}$ .  
 774 Furthermore, the Calcium, Potassium, and hyperpolarization channels have time-dependent gating  
 775 dynamics dependent on steady-state gating variables  $M_\infty$ ,  $N_\infty$  and  $H_\infty$ , respectively.

$$M_\infty = 0.5 \left( 1 + \tanh \left( \frac{x_\alpha - v_1}{v_2} \right) \right) \quad (44)$$

$$\frac{dN}{dt} = \lambda_N (N_\infty - N) \quad (45)$$

$$N_\infty = 0.5 \left( 1 + \tanh \left( \frac{x_\alpha - v_3}{v_4} \right) \right) \quad (46)$$

$$\lambda_N = \phi_N \cosh \left( \frac{x_\alpha - v_3}{2v_4} \right) \quad (47)$$

$$\frac{dH}{dt} = \frac{(H_\infty - H)}{\tau_h} \quad (48)$$

$$H_\infty = \frac{1}{1 + \exp \left( \frac{x_\alpha + v_5}{v_6} \right)} \quad (49)$$

$$\tau_h = 272 - \left( \frac{-1499}{1 + \exp \left( \frac{-x_\alpha + v_7}{v_8} \right)} \right) \quad (50)$$

782 where we set  $v_1 = 0mV$ ,  $v_2 = 20mV$ ,  $v_3 = 0mV$ ,  $v_4 = 15mV$ ,  $v_5 = 78.3mV$ ,  $v_6 = 10.5mV$ ,  
 783  $v_7 = -42.2mV$ ,  $v_8 = 87.3mV$ ,  $v_9 = 5mV$ , and  $v_{th} = -25mV$ . These are the same parameter  
 784 values used in [23].

785 Finally, there is a synaptic gating variable as well:

$$S_\infty = \frac{1}{1 + \exp \left( \frac{v_{th} - x_\alpha}{v_9} \right)} \quad (51)$$

786 When the dynamic gating variables are considered, this is actually a 15-dimensional nonlinear  
 787 dynamical system.

788 In order to measure the frequency of the hub neuron during EPI, the STG model was simulated  
 789 for  $T = 200$  time steps of  $dt = 25ms$ . In EPI, since gradients are taken through the simulation  
 790 process, the number of time steps are kept modest if possible. The chosen  $dt$  and  $T$  were the  
 791 most computationally convenient choices yielding accurate frequency measurement. Poor resolution

afforded by the discrete Fourier transform motivated the use of an alternative basis of complex exponentials to measure spiking frequency. Instead, we used a basis of complex exponentials with frequencies from 0.0-1.0 Hz at 0.01Hz resolution,  $\Phi = [0.0, 0.01, \dots, 1.0]^\top$

Another consideration was that the frequency spectra of the neuron membrane potentials had several peaks. High-frequency sub-threshold activity obscured the maximum frequency measurement in the complex exponential basis. Accordingly, subthreshold activity was set to zero, and the whole signal was low-pass filtered with a moving average window of length 20. The signal was subsequently mean centered. After this pre-processing, the maximum frequency in the filter bank accurately reflected the firing frequency.

Finally, to differentiate through the maximum frequency identification, we used a sum-of-powers normalization. Let  $\mathcal{X}_\alpha \in \mathcal{C}^{|\Phi|}$  be the complex exponential filter bank dot products with the signal  $x_\alpha \in \mathbb{R}^N$ , where  $\alpha \in \{\text{f1}, \text{f2}, \text{hub}, \text{s1}, \text{s2}\}$ . The “frequency identification” vector is

$$v_\alpha = \frac{|\mathcal{X}_\alpha|^\beta}{\sum_{k=1}^N |\mathcal{X}_\alpha(k)|^\beta} \quad (52)$$

The frequency is then calculated as  $\omega_\alpha = v_\alpha^\top \Phi$  with  $\beta = 100$ .

Network syncing, like all other emergent properties in this work, are defined by the emergent property statistics and values. The emergent property statistics are the first- and second-moments of the firing frequencies. The first moments are set to 0.53Hz, while the second moments are set to 0.025Hz<sup>2</sup>:

$$E \begin{bmatrix} \omega_{\text{f1}} \\ \omega_{\text{f2}} \\ \omega_{\text{hub}} \\ \omega_{\text{s1}} \\ \omega_{\text{s2}} \\ (\omega_{\text{f1}} - 0.53)^2 \\ (\omega_{\text{f2}} - 0.53)^2 \\ (\omega_{\text{hub}} - 0.53)^2 \\ (\omega_{\text{s1}} - 0.53)^2 \\ (\omega_{\text{s2}} - 0.53)^2 \end{bmatrix} = \begin{bmatrix} 0.53 \\ 0.53 \\ 0.53 \\ 0.53 \\ 0.53 \\ 0.025^2 \\ 0.025^2 \\ 0.025^2 \\ 0.025^2 \\ 0.025^2 \end{bmatrix} \quad (53)$$

Throughout optimization, the augmented Lagrangian parameters  $\eta$  and  $c$ , were updated after each epoch of 2,500 iterations (see Section B.1.2). The optimization converged after four epochs (Fig. S4).

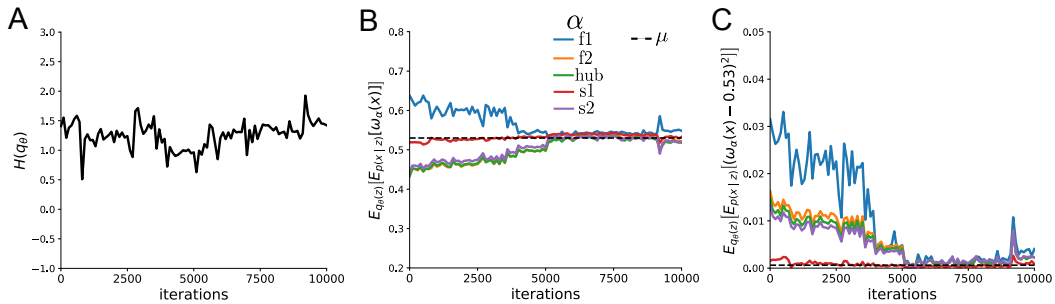


Fig. S4: Emergent property inference of the STG model producing network syncing. A. Entropy throughout optimization. B. The first moment emergent property statistics converge to the emergent property values at 10,000 iterations, following the fourth augmented Lagrangian epoch of 2,500 iterations. (There is no convergence at the end of the third epoch, because  $q_\theta(z)$  failed to produce enough samples yielding  $\omega_{f1}(x)$  less than 0.53Hz.) C. The second moment emergent property statistics converge to the emergent property values.

812 For EPI in Fig 2C, we used a real NVP architecture with four masks and two layers of 10 units per  
 813 mask, and batch normalization momentum of 0.99 mapped onto a support of  $z \in \begin{bmatrix} 4 & 0 \\ 8 & 4 \end{bmatrix}$ .  
 814 We used an augmented Lagrangian coefficient of  $c_0 = 10^2$ , a batch size  $n = 300$ , set  $\nu = 0.1$ , and  
 815 initialized  $q_\theta(z)$  to produce an isotropic Gaussian with mean  $\mu_{\text{init}} = \begin{bmatrix} 6 & 2 \end{bmatrix}$  with standard deviation  
 816  $\sigma_{\text{init}} = 0.5$ .

817 We calculated the Hessian at the mode of the inferred EPI distribution. The Hessian of a proba-  
 818 bility model is the second order gradient of the log probability density  $\log q_\theta(z)$  with respect to the  
 819 parameters  $z$ :  $\frac{\partial^2 \log q_\theta(z)}{\partial z \partial z^\top}$ . With EPI, we can examine the Hessian, which is analytically available  
 820 throughout the deep probability distribution, at a given parameter choice to determine what di-  
 821 mensions of parameter space are sensitive (high magnitude eigenvalue), and which are degenerate  
 822 (low magnitude eigenvalue) with respect to the emergent property produced. In Figure 1B, the  
 823 eigenvectors of the Hessian  $v_1$  and  $v_2$  are shown evaluated at the mode of the distribution. The  
 824 length of the arrows is inversely proportional to the square root of absolute value of their eigen-  
 825 values  $\lambda_1 = -10.8$  and  $\lambda_2 = -2.27$ . We quantitatively measured the sensitivity of the model with  
 826 respect to network syncing along the eigenvectors of the Hessian (Fig. 1B, inset). Sensitivity was  
 827 measured as the slope coefficient of linear regression fit to network syncing error (the sum of squared  
 828 differences of each neuron's frequency from 0.53Hz) as a function of parametric perturbation mag-  
 829 nitude (maximum 0.25) away from the mode along both orientations indicated by the eigenvector  
 830 with 100 equally spaced samples. The sensitivity slope coefficient of eigenvector  $v_1$  with respect to

network syncing was significant ( $\beta = 4.82 \times 10^{-2}$ ,  $p < 10^{-5}$ ) In contrast, eigenvector  $v_2$  did not identify a dimension of parameter space significantly sensitive to network syncing ( $\beta = 8.65 \times 10^{-4}$  with  $p = .67$ ). These sensitivities were compared to all other dimensions of parameter space (100 equally spaced angles from 0 to  $\pi$ ), revealing that the Hessian eigenvectors indeed identified the directions of greatest sensitivity and degeneracy (Fig. 1B, inset).

### 836 B.2.2 Primary visual cortex

837 The dynamics of each neural populations average rate  $x = [x_E \ x_P \ x_S \ x_V]^\top$  are given by:

$$\tau \frac{dx}{dt} = -x + [Wx + h]_+^n \quad (54)$$

838 Some neuron-types largely lack synaptic projections to other neuron-types [43], and it is popular  
839 to only consider a subset of the effective connectivities [24, 44, 45].

$$W = \begin{bmatrix} W_{EE} & W_{EP} & W_{ES} & 0 \\ W_{PE} & W_{PP} & W_{PS} & 0 \\ W_{SE} & 0 & 0 & W_{SV} \\ W_{VE} & W_{VP} & W_{VS} & 0 \end{bmatrix} \quad (55)$$

840 By consolidating information from many experimental datasets, Billeh et al. [47] produce estimates  
841 of the synaptic strength (in mV)

$$M = \begin{bmatrix} 0.36 & 0.48 & 0.31 & 0.28 \\ 1.49 & 0.68 & 0.50 & 0.18 \\ 0.86 & 0.42 & 0.15 & 0.32 \\ 1.31 & 0.41 & 0.52 & 0.37 \end{bmatrix} \quad (56)$$

842 and connection probability

$$C = \begin{bmatrix} 0.16 & 0.411 & 0.424 & 0.087 \\ 0.395 & 0.451 & 0.857 & 0.02 \\ 0.182 & 0.03 & 0.082 & 0.625 \\ 0.105 & 0.22 & 0.77 & 0.028 \end{bmatrix} \quad (57)$$

843 Multiplying these connection probabilities and synaptic efficacies gives us an effective connectivity

844 matrix:

$$W_{\text{full}} = C \odot M = \begin{bmatrix} 0.16 & 0.411 & 0.424 & 0.087 \\ 0.395 & .451 & 0.857 & 0.02 \\ 0.182 & 0.03 & 0.082 & 0.625 \\ 0.105 & 0.22 & 0.77 & 0.028 \end{bmatrix} \quad (58)$$

845 We used the entries of this full effective connectivity matrix that are not considered to be ineffectual  
 846 (Equation 55).

847 We look at how this four-dimensional nonlinear dynamical model of V1 responds to different inputs,  
 848 and compare the predictions of the linear response to the approximate posteriors obtained through  
 849 EPI. The input to the system is the sum of a baseline input  $b = [1 \ 1 \ 1 \ 1]^\top$  and a differential  
 850 input  $dh$ :

$$h = b + dh \quad (59)$$

851 All simulations of this system had  $T = 100$  time points, a time step  $dt = 5\text{ms}$ , and time constant  
 852  $\tau = 20\text{ms}$ . And the system was initialized to a random draw  $x(0)_i \sim \mathcal{N}(1, 0.01)$ .

853 We can describe the dynamics of this system more generally by

$$\dot{x}_i = -x_i + f(u_i) \quad (60)$$

854 where the input to each neuron is

$$u_i = \sum_j W_{ij}x_j + h_i \quad (61)$$

855 Let  $F_{ij} = \gamma_i \delta(i, j)$ , where  $\gamma_i = f'(u_i)$ . Then, the linear response is

$$\frac{dx_{ss}}{dh} = F(W \frac{dx_{ss}}{dh} + I) \quad (62)$$

856 which is calculable by

$$\frac{dx_{ss}}{dh} = (F^{-1} - W)^{-1} \quad (63)$$

857 This calculation is used to produce the magenta lines in Figure 2C, which show the linearly predicted  
 858 inputs that generate a response from two standard deviations (of  $\mathcal{B}$ ) below and above  $y$ .

859 The emergent property we considered was the first and second moments of the change in steady  
 860 state rate  $dx_{ss}$  between the baseline input  $h = b$  and  $h = b + dh$ . We use the following notation to  
 861 indicate that the emergent property statistics were set to the following values:

$$\mathcal{B}(\alpha, y) \triangleq \mathbb{E} \begin{bmatrix} dx_{\alpha,ss} \\ (dx_{\alpha,ss} - y)^2 \end{bmatrix} = \begin{bmatrix} y \\ 0.01^2 \end{bmatrix} \quad (64)$$

862 In the final analysis for this model, we sweep the input one neuron at a time away from the mode  
 863 of each inferred distributions  $dh^* = z^* = \operatorname{argmax}_z \log q_\theta(z \mid \mathcal{B}(\alpha, 0.1))$ . The differential responses  
 864  $\delta x_{\alpha,ss}$  are examined at perturbed inputs  $h = b + dh^* + \delta h_\alpha \hat{u}_\alpha$  where  $\hat{u}_\alpha$  is a unit vector in the  
 865 dimension of  $\alpha$  and  $\delta h_\alpha \in [-15, 15]$ .

866 For each  $\mathcal{B}(\alpha, y)$  with  $\alpha \in \{E, P, S, V\}$  and  $y \in \{0.1, 0.5\}$ , we ran EPI using a real NVP architecture  
 867 of four masks layers with two hidden layers of 10 units, mapped to a support of  $z_i \in [-5, 5]$  with  
 868 no batch normalization. We used an augmented Lagrangian coefficient of  $c_0 = 10^5$ , a batch size  
 869  $n = 1000$ , set  $\nu = 0.5$ . The EPI distributions shown in Fig. 2 are the converged distributions with  
 870 maximum entropy across random seeds.

871 Here, we demonstrate that the algorithm does not necessarily need to start at such an agnostic  
 872 initialization. We set the parameters of the Gaussian initialization  $\mu_{\text{init}}$  and  $\sigma_{\text{init}}$  to the mean and  
 873 covariance of random samples  $z^{(i)} \sim \mathcal{U}(-5, 5)$  that produced emergent property statistic  $dx_{\alpha,ss}$   
 874 within a bound  $\epsilon$  of the emergent property value  $y$ .  $\epsilon = 0.01$  was set to be one standard deviation  
 875 of the emergent property value according to the emergent property value  $0.01^2$  of the variance  
 876 emergent property statistic. This is the only application in the study where such an informed  
 877 initialization was used.

### 878 B.2.3 Superior colliculus

879 In the model of Duan et al [25], there are four total units: two in each hemisphere corresponding to  
 880 the Pro/Contra and Anti/Ipsi populations. They are denoted as left Pro (LP), left Anti (LA), right  
 881 Pro (RP) and right Anti (RA). Each unit has an activity ( $x_\alpha$ ) and internal variable ( $u_\alpha$ ) related  
 882 by

$$x_\alpha = \left( \frac{1}{2} \tanh \left( \frac{u_\alpha - \epsilon}{\zeta} \right) + \frac{1}{2} \right) \quad (65)$$

883 where  $\alpha \in \{LP, LA, RA, RP\}$   $\epsilon = 0.05$  and  $\zeta = 0.5$  control the position and shape of the nonlin-  
 884 earity, respectively.

885 We order the elements of  $x$  and  $u$  in the following manner

$$x = \begin{bmatrix} x_{LP} \\ x_{LA} \\ x_{RP} \\ x_{RA} \end{bmatrix} \quad u = \begin{bmatrix} u_{LP} \\ u_{LA} \\ u_{RP} \\ u_{RA} \end{bmatrix} \quad (66)$$

886 The internal variables follow dynamics:

$$\tau \frac{du}{dt} = -u + Wx + h + \sigma dB \quad (67)$$

887 with time constant  $\tau = 0.09s$  and Gaussian noise  $\sigma dB$  controlled by the magnitude of  $\sigma = 1.0$ . The  
888 weight matrix has 8 parameters  $sW_P$ ,  $sW_A$ ,  $vW_{PA}$ ,  $vW_{AP}$ ,  $hW_P$ ,  $hW_A$ ,  $dW_{PA}$ , and  $dW_{AP}$  (Fig.  
889 4B).

$$W = \begin{bmatrix} sW_P & vW_{PA} & hW_P & dW_{PA} \\ vW_{AP} & sW_A & dW_{AP} & hW_A \\ hW_P & dW_{PA} & sW_P & vW_{PA} \\ dW_{AP} & hW_A & vW_{AP} & sW_A \end{bmatrix} \quad (68)$$

890 The system receives five inputs throughout each trial, which has a total length of 1.8s.

$$h = h_{\text{rule}} + h_{\text{choice-period}} + h_{\text{light}} \quad (69)$$

891 There are rule-based inputs depending on the condition,

$$h_{P,\text{rule}}(t) = \begin{cases} I_{P,\text{rule}} \begin{bmatrix} 1 & 0 & 0 & 1 \end{bmatrix}^\top, & \text{if } t \leq 1.2s \\ 0, & \text{otherwise} \end{cases} \quad (70)$$

$$h_{A,\text{rule}}(t) = \begin{cases} I_{A,\text{rule}} \begin{bmatrix} 0 & 1 & 1 & 0 \end{bmatrix}^\top, & \text{if } t \leq 1.2s \\ 0, & \text{otherwise} \end{cases} \quad (71)$$

893 a choice-period input,

$$h_{\text{choice}}(t) = \begin{cases} I_{\text{choice}} \begin{bmatrix} 1 & 1 & 1 & 1 \end{bmatrix}^\top, & \text{if } t > 1.2s \\ 0, & \text{otherwise} \end{cases} \quad (72)$$

894 and an input to the right or left-side depending on where the light stimulus is delivered.

$$h_{\text{light}}(t) = \begin{cases} I_{\text{light}} \begin{bmatrix} 1 & 1 & 0 & 0 \end{bmatrix}^\top, & \text{if } t > 1.2s \text{ and Left} \\ I_{\text{light}} \begin{bmatrix} 0 & 0 & 1 & 1 \end{bmatrix}^\top, & \text{if } t > 1.2s \text{ and Right} \\ 0, & t \leq 1.2s \end{cases} \quad (73)$$

895 The input parameterization was fixed to  $I_{P,\text{rule}} = 10$ ,  $I_{A,\text{rule}} = 10$ ,  $I_{\text{choice}} = 2$ , and  $I_{\text{light}} = 1$

896 To produce a Bernoulli rate of  $p_{LP}$  in the Left, Pro condition, let  $\hat{p}_i$  be the empirical average steady  
 897 state (ss) response (final  $x_{LP}$  at end of task) over M=500 Gaussian noise draws for a given SC  
 898 model parameterization  $z_i$ :

$$\hat{p}_i = \mathbb{E}_{\sigma dB} [x_{LP} | s = L, c = P, z = z_i] = \frac{1}{M} \sum_{j=1}^M x_{LP}(s = L, c = P, z = z_i, \sigma dB_j) \quad (74)$$

899 where from here on  $x_\alpha$  denotes the steady state activity at the end of the trial. For the first  
 900 emergent property statistic, the average over EPI samples (from  $q_\theta(z)$ ) is set to the desired value  
 901  $p_{LP}$ :

$$\mathbb{E}_{z_i \sim q_\phi} [\mathbb{E}_{\sigma dB} [x_{LP,ss} | s = L, c = P, z = z_i]] = \mathbb{E}_{z_i \sim q_\phi} [\hat{p}_i] = p_{LP} \quad (75)$$

902 For the next emergent property statistic, we ask that the variance of the steady state responses  
 903 across Gaussian draws, is the Bernoulli variance for the empirical rate  $\hat{p}_i$ .

$$\mathbb{E}_{z \sim q_\phi} [\sigma_{err}^2] = 0 \quad (76)$$

904

$$\sigma_{err}^2 = Var_{\sigma dB} [x_{LP} | s = L, c = P, z = z_i] - \hat{p}_i(1 - \hat{p}_i) \quad (77)$$

905 We have an additional constraint that the Pro neuron on the opposite hemisphere should have the  
 906 opposite value (0 and 1). We can enforce this with a final constraint:

$$\mathbb{E}_{z \sim q_\phi} [d_P] = \mathbb{E}_{\sigma dB} [(x_{LP} - x_{RP})^2 | s = L, c = P, z = z_i] = 1 \quad (78)$$

907 Since the maximum variance of a random variable bounded from 0 to 1 is the Bernoulli variance  
 908  $\hat{p}(1 - \hat{p})$ , and the maximum squared difference between two variables bounded from 0 to 1 is 1, we  
 909 do not need to control the second moment of these test statistics. In practice, these variables are  
 910 dynamical system states and can only exponentially decay (or saturate) to 0 (or 1), so the Bernoulli  
 911 variance error and squared difference constraints can only be undershot. This is important to be  
 912 mindful of when evaluating the convergence criteria. Instead of using our usual hypothesis testing  
 913 criteria for convergence to the emergent property, we set a slack variable threshold only for these  
 914 technically infeasible emergent property values to 0.05.

915 Training DSNs to learn distributions of dynamical system parameterizations that produce Bernoulli  
 916 responses at a given rate (with small variance around that rate) was harder to do than expected.  
 917 There is a pathology in this optimization setup, where the learned distribution of weights is bimodal  
 918 attributing a fraction  $p$  of the samples to an expansive mode (which always sends  $x_{LP}$  to 1), and a  
 919 fraction  $1 - p$  to a decaying mode (which always sends  $x_{LP}$  to 0). This pathology was avoided using

- 920 an inequality constraint prohibiting parameter samples that resulted in low variance of responses  
 921 across noise.
- 922 In total, the emergent property of rapid task switching at accuracy level  $p$  was defined as

$$\mathcal{B}(p) \triangleq \mathbb{E} \begin{bmatrix} \hat{p}_P \\ \hat{p}_A \\ (\hat{p}_P - p)^2 \\ (\hat{p}_A - p)^2 \\ \sigma_{P,err}^2 \\ \sigma_{A,err}^2 \\ d_P \\ d_A \end{bmatrix} = \begin{bmatrix} p \\ p \\ 0.15^2 \\ 0.15^2 \\ 0 \\ 0 \\ 1 \\ 1 \end{bmatrix} \quad (79)$$

- 923 For each accuracy level  $p$ , we ran EPI for 10 different random seeds using an architecture of 10  
 924 planar flows with a support of  $z \in \mathbb{R}^8$ . We used an augmented Lagrangian coefficient of  $c_0 = 10^2$ , a  
 925 batch size  $n = 300$ , and set  $\nu = 0.5$ , and initialized  $q_\theta(z)$  to produce an isotropic Gaussian of zero  
 926 mean with standard deviation  $\sigma_{\text{init}} = 1$ . The EPI distributions shown in Fig. 4 are the converged  
 927 distributions with maximum entropy across random seeds.

#### 928 B.2.4 Rank-1 RNN

- 929 Recent work establishes a link between RNN connectivity weights and the resulting dynamical  
 930 responses of the network, using dynamic mean field theory (DMFT) [26]. Specifically, DMFT  
 931 describes the properties of activity in infinite-size neural networks given a distribution on the  
 932 connectivity weights. In such a model, the connectivity of a rank-1 RNN (which was sufficient for  
 933 the Gaussian posterior conditioning task), has weight matrix  $W$ , which is the sum of a random  
 934 component with strength determined by  $g$  and a structured component determined by the outer  
 935 product of vectors  $m$  and  $n$ :

$$W = g\chi + \frac{1}{N}mn^\top, \quad (80)$$

- 936 where  $\chi_{ij} \sim \mathcal{N}(0, \frac{1}{N})$ , and the entries of  $m$  and  $n$  are drawn from Gaussian distributions  $m_i \sim$   
 937  $\mathcal{N}(M_m, 1)$  and  $n_i \sim \mathcal{N}(M_n, 1)$ . From such a parameterization, this theory produces consistency  
 938 equations for the dynamic mean field variables in terms of parameters like  $g$ ,  $M_m$ , and  $M_n$ , which we  
 939 study in Section 3.5. That is the dynamic mean field variables (e.g. the activity along a vector  $\kappa_v$ ,  
 940 the total variance  $\Delta_0$ , structured variance  $\Delta_\infty$ , and the chaotic variance  $\Delta_T$ ) are written as functions

of one another in terms of connectivity parameters. The values of these variables can be used obtained using a nonlinear system of equations solver. These dynamic mean field variables are then cast as task-relevant variables with respect to the context of the provided inputs. Mastrogiovisepp et al. designed low-rank RNN connectivities via minimalist connectivity parameters to solve canonical tasks from behavioral neuroscience.

We consider the DMFT equation solver as a black box that takes in a low-rank parameterization  $z$  (e.g.  $z = [g \ M_m \ M_n]$ ) and outputs the values of the dynamic mean field variables, of which we cast  $\kappa_r$  and  $\Delta_T$  as task-relevant variables  $\mu_{\text{post}}$  and  $\sigma_{\text{post}}^2$  in the Gaussian posterior conditioning toy example. Importantly, the solution produced by the solver is differentiable with respect to the input parameters, allowing us to use DMFT to calculate the emergent property statistics in EPI to learn distributions on such connectivity parameters of RNNs that execute tasks.

Specifically, we solve for the mean field variables  $\kappa_r$ ,  $\kappa_n$ ,  $\Delta_0$  and  $\Delta_\infty$ , where the readout is nominally chosen to point in the unit orthant  $r = [1 \ \dots \ 1]^\top$ . The consistency equations for these variables in the presence of a constant input  $h = y - (n - M_n)$  can be derived following [26] are

$$\begin{aligned} \kappa_r &= G_1(\kappa_r, \kappa_n, \Delta_0, \Delta_\infty) = M_m \kappa_n + y \\ \kappa_n &= G_2(\kappa_r, \kappa_n, \Delta_0, \Delta_\infty) = M_n \langle [\phi_i] \rangle + \langle [\phi'_i] \rangle \\ \frac{\Delta_0^2 - \Delta_\infty^2}{2} &= G_3(\kappa_r, \kappa_n, \Delta_0, \Delta_\infty) = g^2 \left( \int \mathcal{D}z \Phi^2(\kappa_r + \sqrt{\Delta_0} z) - \int \mathcal{D}z \int \mathcal{D}x \Phi(\kappa_r + \sqrt{\Delta_0 - \Delta_\infty} x + \sqrt{\Delta_\infty} z) \right) \\ &\quad + (\kappa_n^2 + 1)(\Delta_0 - \Delta_\infty) \\ \Delta_\infty &= G_4(\kappa_r, \kappa_n, \Delta_0, \Delta_\infty) = g^2 \int \mathcal{D}z \left[ \int \mathcal{D}x \phi(\kappa_r + \sqrt{\Delta_0 - \Delta_\infty} x + \sqrt{\Delta_\infty} z) \right]^2 + \kappa_n^2 + 1 \end{aligned} \tag{81}$$

where here  $z$  is a gaussian integration variable. We can solve these equations by simulating the following Langevin dynamical system to a steady state.

$$\begin{aligned} l(t) &= \frac{\Delta_0(t)^2 - \Delta_\infty(t)^2}{2} \\ \Delta_0(t) &= \sqrt{2x(t) + \Delta_\infty(t)^2} \\ \frac{d\kappa_r(t)}{dt} &= -\kappa_r(t) + F(\kappa_r(t), \kappa_n(t), \Delta_0(t), \Delta_\infty(t)) \\ \frac{d\kappa_n(t)}{dt} &= -\kappa_n + G(\kappa_r(t), \kappa_n(t), \Delta_0(t), \Delta_\infty(t)) \\ \frac{dl(t)}{dt} &= -l(t) + H(\kappa_r(t), \kappa_n(t), \Delta_0(t), \Delta_\infty(t)) \\ \frac{d\Delta_\infty(t)}{dt} &= -\Delta_\infty(t) + L(\kappa_r(t), \kappa_n(t), \Delta_0(t), \Delta_\infty(t)) \end{aligned} \tag{82}$$

957 Then, the chaotic variance, which is necessary for the Gaussian posterior conditioning example, is  
 958 simply calculated via

$$\Delta_T = \Delta_0 - \Delta_\infty \quad (83)$$

959 We ran EPI using a real NVP architecture of two masks and two layers per mask with 10 units  
 960 mapped to a support of  $z \in \left[ \begin{bmatrix} 0 & -5 & -5 \end{bmatrix}, \begin{bmatrix} 5 & 5 & 5 \end{bmatrix} \right]$  with no batch normalization. We used  
 961 an augmented Lagrangian coefficient of  $c_0 = 1$ , a batch size  $n = 300$ , set  $\nu = 0.2$ , and initialized  
 962  $q_\theta(z)$  to produce an isotropic Gaussian with mean  $\mu_{\text{init}} = \begin{bmatrix} 2.5 & 0 & 0 \end{bmatrix}$  with standard deviation  
 963  $\sigma_{\text{init}} = 2.0$ . The EPI distributions shown in Fig. 4 are the converged distributions with maximum  
 964 entropy across five random seeds.

965 In addition to the Gaussian posterior conditioning example in Section 3.5, we modeled two tasks  
 966 from Mastrogiuseppe et al.: noisy detection and context-dependent discrimination. We used the  
 967 same theoretical equations and task setups described in their study.

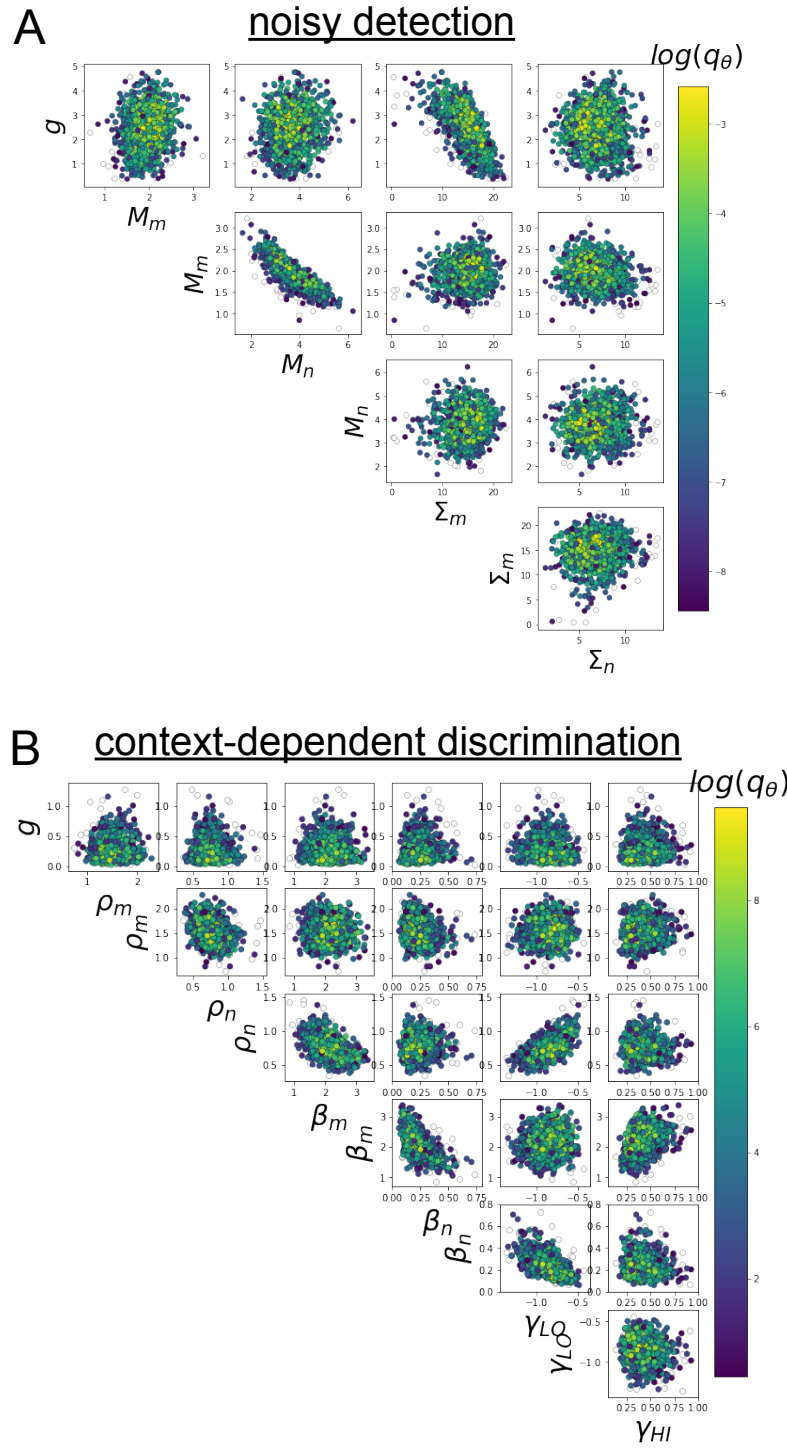


Fig. S5: A. EPI for rank-1 networks doing noisy discrimination. B. EPI for rank-2 networks doing context-dependent discrimination. See [26] for theoretical equations and task description.